remote sensing

MDPI

Review

A Systematic Review of the Application of the Geostationary Ocean Color Imager to the Water Quality Monitoring of Inland and Coastal Waters

Shidi Shao [1,2], Yu Wang [3], Ge Liu [1,*] and Kaishan Song [1]

[1] Northeast Institute of Geography and Agroecology, Chinese Academy of Sciences, Changchun 130102, China; shaoshidi@iga.ac.cn (S.S.); songkaishan@iga.ac.cn (K.S.)
[2] University of Chinese Academy of Sciences, Beijing 100049, China
[3] Center for Satellite Application on Ecology and Environment, Ministry of Ecology and Environment of the People's Republic of China, Beijing 100029, China; wangyusecmep1220@163.com
* Correspondence: liuge@iga.ac.cn

Abstract: In recent decades, eutrophication in inland and coastal waters (ICWs) has increased due to anthropogenic activities and global warming, thus requiring timely monitoring. Compared with traditional sampling and laboratory analysis methods, satellite remote sensing technology can provide macro-scale, low-cost, and near real-time water quality monitoring services. The Geostationary Ocean Color Imager (GOCI), aboard the Communication Ocean and Meteorological Satellite (COMS) from the Republic of Korea, marked a significant milestone as the world's inaugural geostationary ocean color observation satellite. Its operational tenure spanned from 1 April 2011 to 31 March 2021. Over ten years, the GOCI has observed oceans, coastal waters, and inland waters within its 2500 km × 2500 km target area centered on the Korean Peninsula. The most attractive feature of the GOCI, compared with other commonly used water color sensors, was its high temporal resolution (1 h, eight times daily from 0 UTC to 7 UTC), providing an opportunity to monitor ICWs, where their water quality can undergo significant changes within a day. This study aims to comprehensively review GOCI features and applications in ICWs, analyzing progress in atmospheric correction algorithms and water quality monitoring. Analyzing 123 articles from the Web of Science and China National Knowledge Infrastructure (CNKI) through a bibliometric quantitative approach, we examined the GOCI's strength and performance with different processing methods. These articles reveal that the GOCI played an essential role in monitoring the ecological health of ICWs in its observation coverage (2500 km × 2500 km) in East Asia. The GOCI has led the way to a new era of geostationary ocean satellites, providing new technical means for monitoring water quality in oceans, coastal zones, and inland lakes. We also discuss the challenges encountered by Geostationary Ocean Color Sensors in monitoring water quality and provide suggestions for future Geostationary Ocean Color Sensors to better monitor the ICWs.

Keywords: GOCI; inland and coastal waters; atmospheric correction; algal blooms; water quality parameters

Citation: Shao, S.; Wang, Y.; Liu, G.; Song, K. A Systematic Review of the Application of the Geostationary Ocean Color Imager to the Water Quality Monitoring of Inland and Coastal Waters. *Remote Sens.* **2024**, *16*, 1623. https://doi.org/10.3390/rs16091623

Academic Editor: Andrew Clive Banks

Received: 25 March 2024
Revised: 27 April 2024
Accepted: 29 April 2024
Published: 1 May 2024

1. Introduction

Water accounts for about 74% of Earth's surface. Water is an important carrier and critical factor in studying the energy exchange of surface materials [1,2]. For research convenience in water color remote sensing, the Earth's water is usually divided into Case I and Case II waters based on the optical properties of water [3–5]. The optical properties of Case I waters (open oceans) are mainly determined by phytoplankton. Case II waters, including inland and coastal waters (denoted as ICWs; all abbreviations or symbols in this study are shown in Table 1 and Table S1), are optical complexes determined by phytoplankton, detritus, and colored dissolved organic matter (CDOM) [6,7]. Most of the

Earth's population lives near ICWs, making them the most economically and socially active regions on Earth. Large quantities of nutrients and pollutants released by human activities are entering various ICWs globally, disrupting their ecological equilibrium. Damaged waterbodies will, in turn, threaten human health and lead to economic losses [8–13]. Remote sensing technology can complement traditional field sampling and laboratory analysis methods by targeting optically active substance concentrations in monitoring water quality, using reflectance signals. With the growing number of water color satellite sensors launched in recent decades, numerous algorithms have been proposed to retrieve water quality parameters from satellite images to monitor ICWs.

Table 1. Abbreviations and symbols used in this study.

Abbreviations or Symbols		Abbreviations or Symbols	
ABs	Algal blooms	OSMI	Ocean Scanning Multispectral Imager
AFAI	Alternative floating algae index	OE	*Optics EXPRESS*
AC	Atmospheric correction	POC	Particulate organic carbon
CNKI	China National Knowledge Infrastructure	PC	Phycocyanin
Chla	Chlorophyll a	RF	Random forest
CDOM	Colored dissolved organic matter	$L_{rc}(\lambda)$	Rayleigh-corrected radiance
CBI	Cyanobacterial bloom intensity	RI	Red tide index
k_d	Diffuse attenuation coefficient	RS	*Remote Sensing*
DOC	Dissolved organic carbon	RSE	*Remote Sensing of Environment*
FAC	Floating algae cover	$R_{rs}(\lambda)$	Remote sensing reflectance
FLH	Fluorescence line height	Sci Total Environ	*Science of the Total Environment*
GABI	Generalized algal bloom index algorithm	SIA	Sea ice area
GLI	Generation Global Imager	SIT	Sea ice thickness
GLIMR	Geostationary Littoral Imaging and Monitoring Radiometer	SSCs	Sea surface currents
HABs	Harmful algal blooms	SSS	Sea surface salinity
IEEE T-GRS	IEEE Transactions on Geoscience and Remote Sensing	SDD	Secchi disk depth
ICWs	Inland and coastal waters	SGLI	Second Generation Global Imager
JAG	*International Journal of Applied Earth Observation and Geoinformation*	SWIR	Shortwave infrared
Int J Remote Sens	*International Journal of Remote Sensing*	SZA	Solar zenith angle
ISPRS	*ISPRS Journal of Photogrammetry and Remote Sensing*	SPM	Suspended particulate matter
LCI	Linear Combination Index	SCI	Synthetic chlorophyll index
MERIS	Medium-Resolution Imaging Spectrometer Instrument	GOCI	The Geostationary Ocean Color Imager
MODIS	Moderate-Resolution Imaging Spectroradiometer	UV	Ultraviolet
NASA	National Aeronautics and Space Administration	VIIRS	Visible Infrared Imaging Radiometer
NIR	Near-infrared	WR	*Water Research*
NPP	Net primary production	YRE	Yalu River estuary
NDVI	Normalized difference vegetation index	YOC	Yellow and East China Sea Ocean Color
NRTI	Normalized red tide index		

Remote sensing of water color from space began in 1978 with the successful launch of the Coastal Zone Color Scanner (CZCS) by the National Aeronautics and Space Administration (NASA) [14]. The CZCS, an experimental radiometer intended to operate for only one year, had six bands ranging from visible to near-infrared (NIR). The CZCS provided valuable experience for subsequent water color satellite development [15–17]. After ten years, several water color sensors were launched, including the Maritime Observation Satellite (MOS) and Ocean Color and Temperature Scanner (OCTS), as well as the Polarization and Directionality of the Earth's Reflectances (POLDER) instrument in 1996 and the Sea-viewing Wide Field-of-view Sensor (SeaWiFS) in 1997. The SeaWiFS was the first water color sensor that could provide continuous data on the bio-optical properties (i.e., those properties of organisms that can be visually recorded) of the oceans [18–20]. In 1999, the United States successfully launched the Moderate Resolution Imaging Spectroradiometer (MODIS) on the Terra satellite, the first advanced polar-orbiting environmental remote-sensing satellite with nine specific water color bands from 412 to 865 nm. MODIS also had three shortwave infrared (SWIR) bands (1240, 1640, and 2130 nm), which had very low reflectance due to the high absorption of pure water [21,22]. The SWIR-based atmospheric correction (AC) method is critical for obtaining reliable and high-accuracy remote sensing reflectance ($R_{rs}(\lambda)$) products of highly turbid ICWs. In 2002, the MODIS sensor on the Aqua satellite was launched and began to observe the Earth along with MODIS from Terra (Terra in the morning, Aqua in the afternoon), providing continuous

water color observations. MODIS has been the most critical water color satellite of the past two decades [23–28]. The Visible Infrared Imaging Radiometer (VIIRS) extends and enhances the AVHRR and MODIS observation series with six water color wavelengths. The three VIIRS sensors (Suomi-NPP, NOAA-20, and NOAA-21) were launched in 2011, 2017, and 2022, respectively. Since VIIRS has spectral bands similar to MODIS, the water quality parameters that MODIS can extract or derive can also be directly monitored by VIIRS. VIIRS can provide water color products for highly turbid ICWs, improving the observations capabilities of MODIS, whose water color bands tend to saturate [29–34]. In December 2018, the United States launched SeaHawk-1, a CubeSat (small, cube-shaped satellites) fitted with a low-cost, miniature ocean color sensor called HawkEye that enables fine spatial resolution observations of the ocean [35].

The Medium-Resolution Imaging Spectrometer Instrument (MERIS) is a sensor deployed in March of 2002 onboard the polar-orbiting Envisat-1 environmental research satellite by the European Space Agency (ESA). The most significant advantage of MERIS is its various water color band selections (fifteen bands from 412 to 900 nm). For example, the 620 nm band can be used to estimate cyanobacteria biomass in ICWs by targeting 86 characteristic pigments (phycocyanin (PC)) [36–38]. The Sentinel-3 Ocean and Land Colour Instrument (OLCI) is based on ENVISAT MERIS's opto-mechanical and imaging design and was launched in 2016 (S3A) and 2018 (S3B). The OLCI presents many improvements compared with MERIS, such as an increase in the number of spectral bands (from 15 to 21), mitigation of sun-glint contamination by tilting cameras in the westerly direction, and increased coverage of global ocean (<4 days) and land (<3 days with one satellite, ignoring the effect of clouds), compared to MERIS, which is approximately 15 days [39–42].

In addition to the United States and the European Union, other countries, such as Japan, China, India, and South Korea, have also released satellites with water color bands. Japan launched the ocean color satellite Advanced Earth Observation Satellite (ADEOS) in 1996. ADEOS had twelve bands in the wavelength range of 400–900 nm with a spatial resolution of 700 m [43–45]. Japan launched the ADEOS-II satellite with the Generation Global Imager (GLI) sensor, with thirty-three bands in the 375–12500 nm wavelength range in 2002. Among these thirty-three bands, six had a spatial resolution of 250 m. The Second-Generation Global Imager (SGLI) satellite is an Earth observation satellite developed by the Japan Aerospace Exploration Agency (JAXA) and launched in 2017. The SGLI can observe 19 bands of radiation from ultraviolet (UV) to the thermal infrared region (380 nm–12 µm). The SGLI has two polarization channels (673.5 and 868.5 nm) [46–48]. Since 2002, China has launched a series of ocean water color satellites, including HY-1A (2002), HY-1B (2007), HY-1C (2018), HY-1D (2022), and HY-1E (2023). The water color bands of the early HY satellite series (e.g., HY-1A, HY-1B) are very close to the MODIS water color bands. Starting from HY-1C, the HY series satellites have specific water color bands (e.g., UV bands). The recently launched HY-1E has two sensors, Chinese Ocean Color and Temperature Scanner 2 (COCTS2) (with eighteen bands and a one-day revisit cycle) and Playful Magnetic Resonance Imaging Simulator (PMRIS) (with nineteen bands and a three-day revisit cycle) [49,50]. India has launched several water color satellites, including Oceansat-1 (1996), Oceansat-2 (2009), and Oceansat-3 (2022). The bands have increased from eight (Oceansat-1) to thirteen bands with a spatial resolution of 360 m (Oceansat-3) [51–53]. The Ocean Scanning Multispectral Imager (OSMI), mounted on the polar-orbiting satellite Korea Multi-Purpose Satellite-1 (KOMPSAT-1), was launched by South Korea in 1999. OSMI was launched in 2010 and had six bands in the 400–900 nm wavelength range and a spatial resolution of 1 km [54,55].

The Geostationary Ocean Color Imager (GOCI) was the world's first geostationary water color satellite. It was positioned in a geostationary orbit at approximately 128.2 degrees east longitude, providing continuous monitoring of the oceanic and ICW conditions over the East Asian region. Subsequently, South Korea launched the GOCI-II in 2020. The GOCI-II has many improvements over the GOCI, with more water color bands and higher spatial resolution [56–58].

Compared with MODIS, VIIRS, or other commonly used water color sensors, the most attractive characteristic of the GOCI was its high temporal resolution (1 h, eight times daily from 0 UTC to 7 UTC), which is important for the accurate monitoring of water quality, which can change on an hourly or even sub-hourly basis in ICWs [19,59–63]. The GOCI was the first sensor with the ability to continuously monitor water quality variations in the ICWs with an hourly temporal resolution. The GOCI provided images to monitor the water quality of oceans and ICWs in its target area (about 2500 km × 2500 km centered on the Korean Peninsula) for nearly ten years, from the first image in 2011 to 2021, when it stopped observations.

Systematic reviews of the research progress and challenges in applying the GOCI to inland coastal waters (ICWs) have been scarcely documented until now [64–69]. Many countries have launched or plan to launch geostationary water color satellites such as the GOCI-II and the Geostationary Littoral Imaging and Monitoring Radiometer (GLIMR) [62]. The insights garnered by reviewing the GOCI's functionality have helped design sensors and construct water quality algorithms. This study aims to comprehensively review the GOCI, providing information on the configuration parameters of the GOCI sensor, an overview of the GOCI, an AC algorithm, AB monitoring, estimation of water quality parameters (chlorophyll a (Chla), suspended particulate matter (SPM), water clarity. In addition, we also reviewed other parameters such as CDOM, particulate organic carbon (POC), dissolved organic carbon (DOC), net primary production (NPP), sea surface salinity (SSS), sea surface currents (SSCs), sea ice, sea fog, lake ice, and the diffuse attenuation coefficient (k_d), etc.). We also discuss advantages and disadvantages as well as future trends (Figure 1). We compare its spatial and temporal resolutions with those of MODIS, Landsat, Sentinel, and other water color satellites, highlighting the high observation frequency of the GOCI in Table 2.

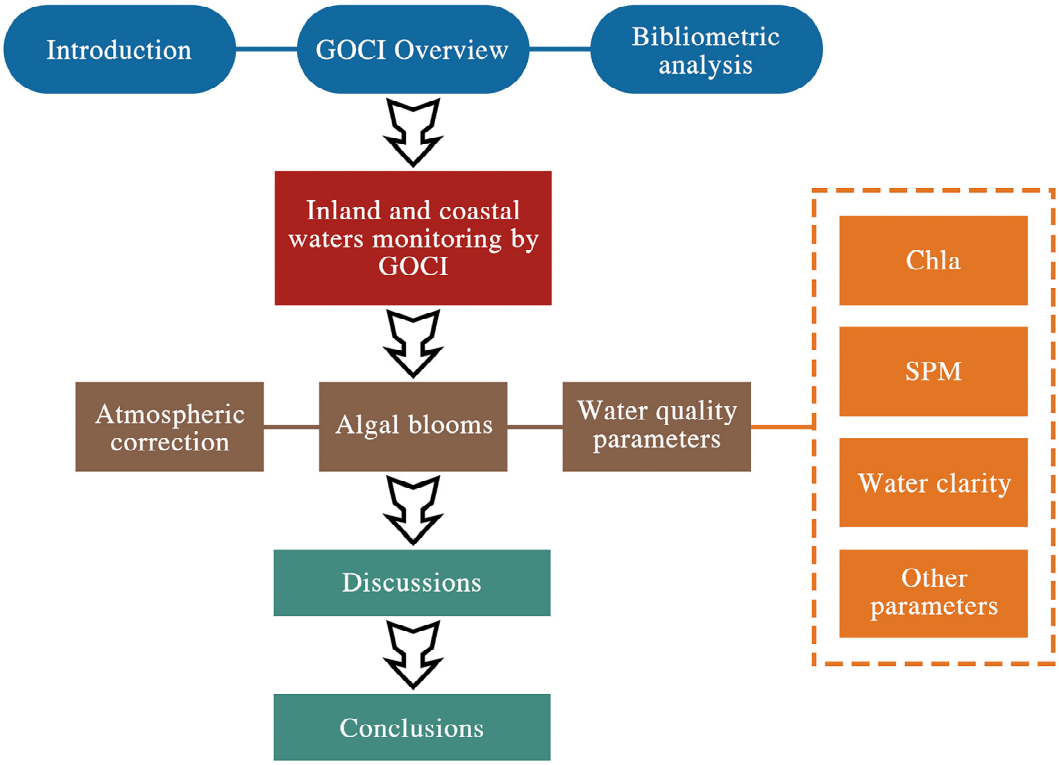

Figure 1. Structure of this paper.

Table 2. Comparison of spatial and temporal resolutions of typical water color remote sensing satellites and their launch dates.

Number	Data	Spatial Resolution (m)	Temporal Resolution	Launched Time
1	CZCS	1000	One day	1978
2	SeaWiFS	1100, 4500	One day	1997
3	MODIS_TERRA	250, 500, 1000	One day	1999
4	MODIS_AQUA	250, 500, 1000	One day	2002
5	VIIRS Suomi NPP	375, 750	One day	2011
6	VIIRS NOAA-20	375, 750	One day	2017
7	VIIRS NOAA-21	375, 750	One day	2021
8	MERIS	300, 1200	Three days	2002
9	Sentinel-3A OLCI	300	<Two days	2016
10	Sentinel-3B OLCI	300	<Two days	2018
11	ADEOS	700	Ten days	1996
12	ADEOS-II	250, 1000	Four days	2002
13	SGLI	250	One day	2017
14	HY-1A	250	Three days/Seven days	2002
15	HY-1B	250	One day/Seven days	2007
16	HY-1C	250	One day/Three days	2018
17	HY-1D	250	One day/Three days	2022
18	HY-1E	100	One day/Three days	2023
19	Oceansat-1	360	Two days	1996
20	Oceansat-2	360	Two days	2009
21	Oceansat-3	360	One day/Three days	2022
22	OSMI	1000	Three days	1999
23	GOCI	500	One hour	2010
24	GOCI-II	250	One hour	2020

2. GOCI Overview

The Communication Ocean and Meteorological Satellite (COMS), launched in 2010, is South Korea's first geostationary orbit meteorological satellite and was designed for meteorological services and ocean monitoring research. It was equipped with a new generation of GOCI sensors, which acquired data in eight bands (including six visible light bands and two NIR bands), as shown in Table 3. Its main advantage was to provide satellite observation of the target area eight times daily, from 0 UTC to 7 UTC. Real-time monitoring was centered on South Korea (36°N 130°E) and also encompassed North Korea, Japan, Russia, and China, including the Bohai Sea, the Yellow Sea, and the East China Sea (Figure 2). The total coverage area was about 2500 km × 2500 km [70].

Table 3. GOCI bands and configuration parameter information.

Bands	Center Wavelength/nm	Band Width/nm	Spectrum Type	Signal-to-Noise Ratio
B1	412	20	VIS	1077
B2	443	20	VIS	1199
B3	490	20	VIS	1316
B4	555	20	VIS	1223
B5	660	20	VIS	1192
B6	680	10	VIS	1093
B7	745	20	NIR	1107
B8	865	40	NIR	1009

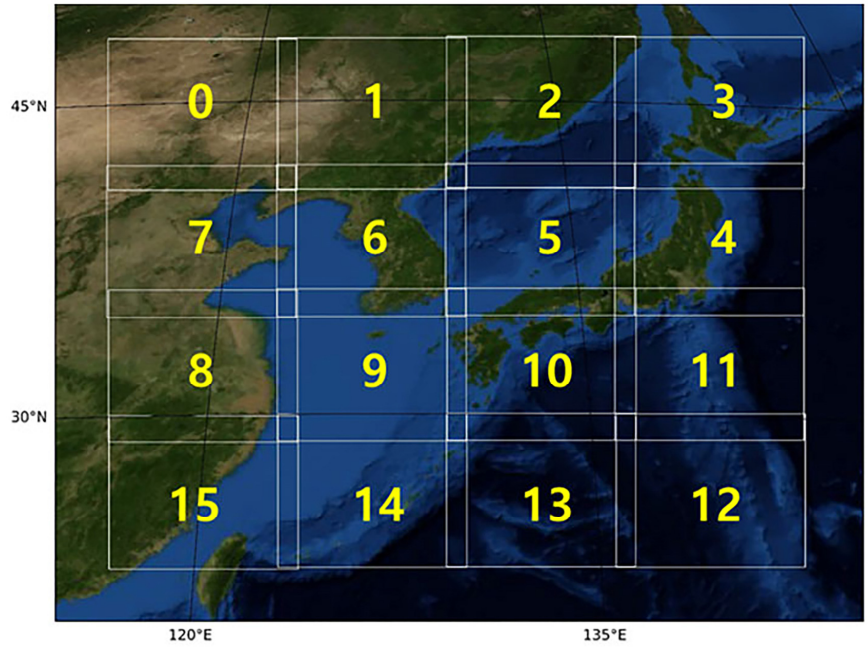

Figure 2. The regional observation area of GOCI (https://kosc.kiost.ac.kr/index.nm?menuCd=43&lang=en, accessed on 25 January 2024).

The GOCI has fulfilled its mission for nearly a decade by playing a significant role in ICW monitoring. The GOCI-II, which succeeded the GOCI, was launched in February 2020 and has up to 13 bands (Table 4). Moreover, the GOCI-II has a spatial resolution of up to 250 m, generating ten views of imagery a day (23 UTC to 8 UTC) [71].

Table 4. Band parameters information for GOCI-II.

Band	Wavelength/nm	Bandwidth/nm	Primary Use
B1	380	20	CDOM
B2	412	20	CDOM, Chla
B3	443	20	Chla absorption maximum
B4	490	20	Chla, other pigments
B5	510	20	Chla, absorbing aerosol in ocean waters
B6	555	20	Turbidity, SPM
B7	620	20	Detect phytoplankton species
B8	660	20	Baseline of fluorescence signal, Chla, SPM
B9	680	10	Fluorescence signal
B10	709	10	Fluorescence base signal, AC, SPM
B11	745	20	AC, vegetation index
B12	865	40	AC, aerosol optical depth
B13	PAN	483	/

3. Bibliometric Analysis

Over the last decade, the GOCI has been increasingly used in remote sensing monitoring research of ICWs due to its advantages and development potential, with a surge in research papers. Our bibliometric analysis, based on Web of Science queries with "GOCI" and "remote sensing" as keywords, retrieved a total of 164 papers, of which 123 met eligibility criteria. The number of publications showed a steady increase, starting from 4 papers published in 2010 to a peak of 13 in 2021 and 2022 (Figure 3 and Table S2). The study areas mentioned in these papers are summarized in Figure 4. Additionally, we find that articles have been published in more than 40 journals, of which 36 were published in *Remote Sensing* (RS); followed by 16 in *Remote Sensing of the Environment* (RSE); 7 in the *Ocean Science Journal* (Ocean Sci J); 6 in *Optics EXPRESS* (OE); 4 in the *Science of the*

Total Environment (Sci Total Environ), *International Journal of Remote Sensing* (Int J Remote Sens), and *Environmental Science and Pollution Research* (Environ Sci Pollut Res); and 3 in *Sensors*, *ISPRS Journal of Photogrammetry and Remote Sensing* (ISPRS), and *IEEE Transaction on Geoscience and Remote Sensing* (IEEE T-GRS) (Figure 5).

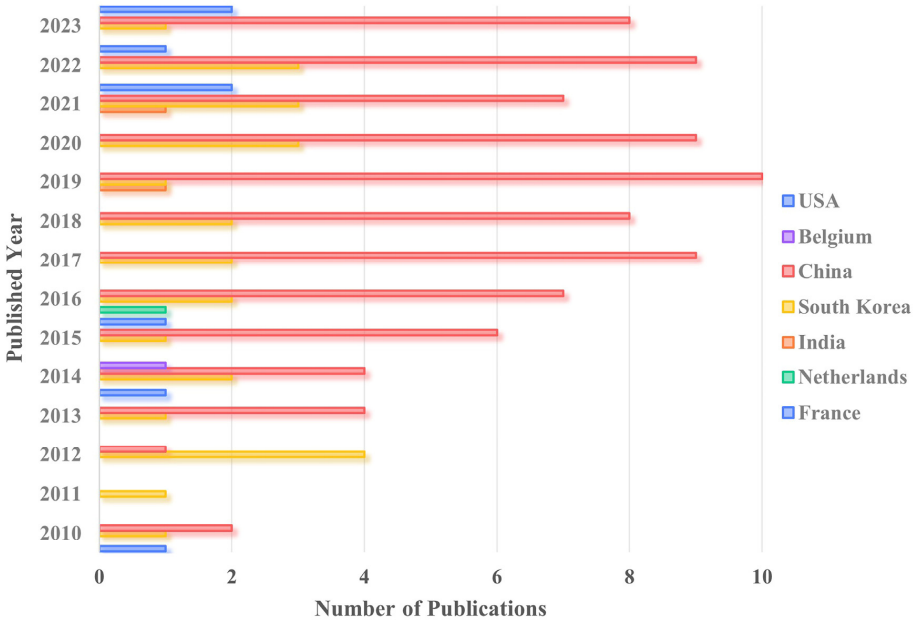

Figure 3. Number and countries of papers published related to GOCI between 2010 and 2023.

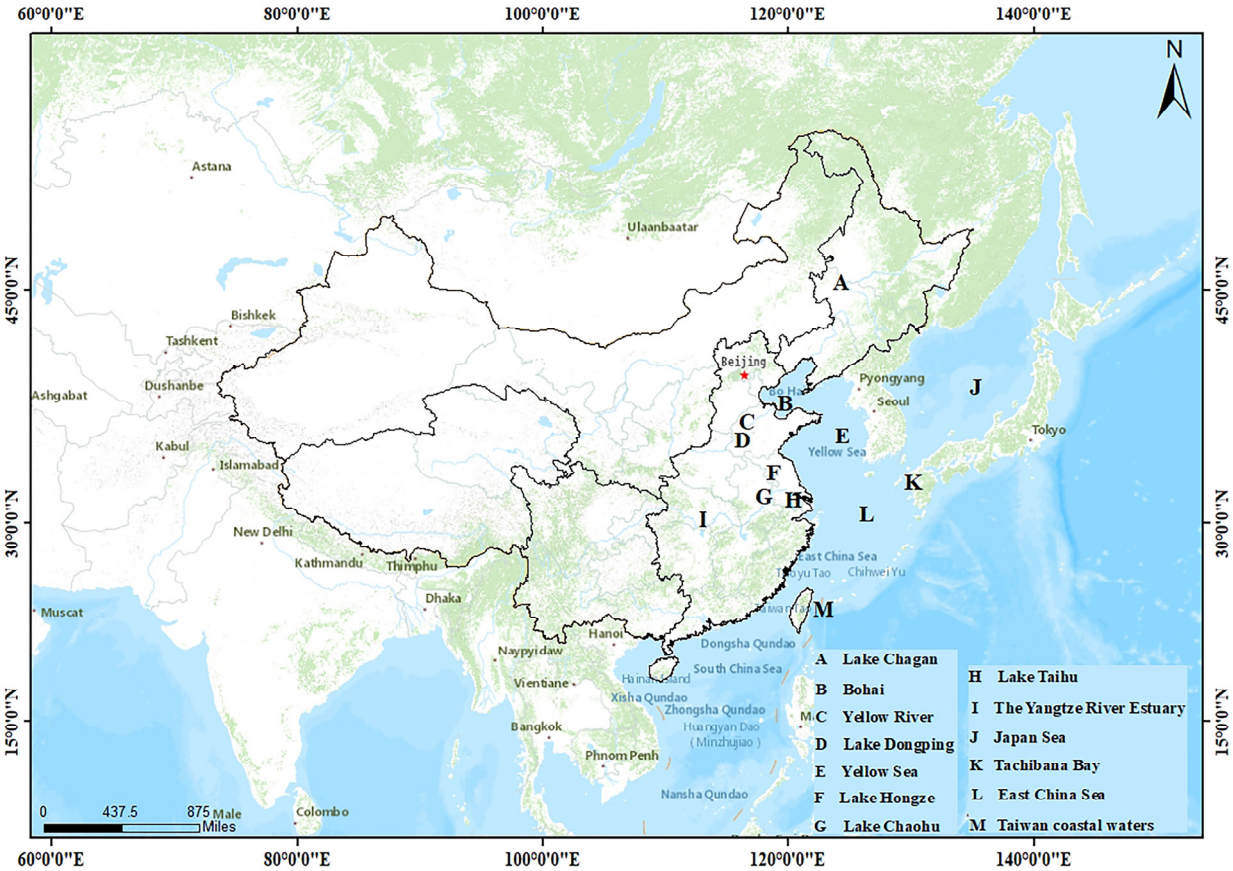

Figure 4. Map of the study area.

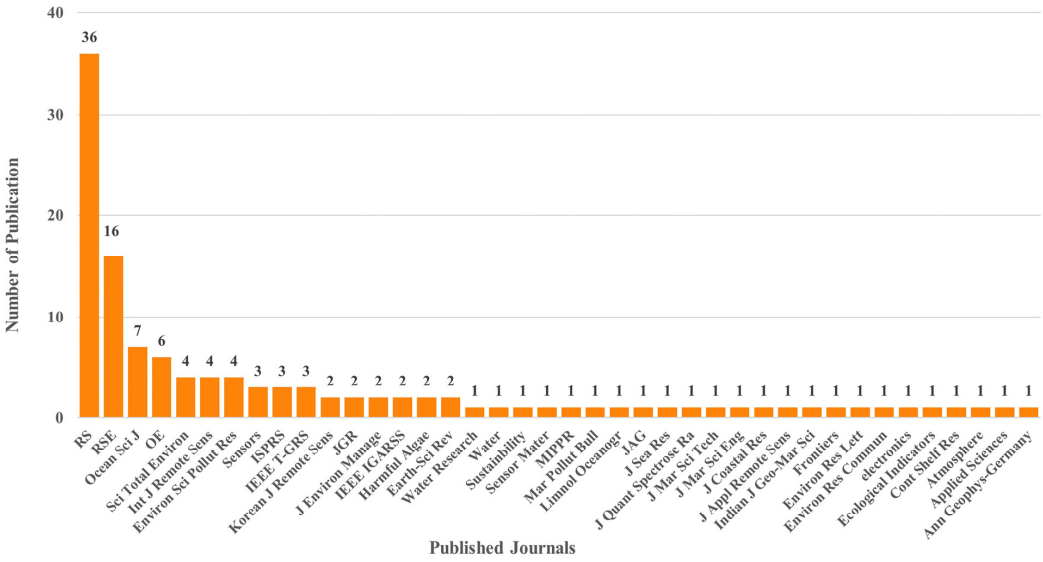

Figure 5. Journals and number of publications.

Using "GOCI", "remote sensing," and "inland and coastal waters" as the subject terms in the "Web of Science" search, we retrieved a total of 1546 eligible authors from the core collection. A VOSviewer statistical analysis of keywords using "author name" was used to form a keyword map (Figure 6). The authors with the highest number of occurrences were Kim, Jhoon, Ryu, and Joo-hyung, totaling 36 occurrences. The highest number of citations was 1090. Recognizing the significant contributions of Chinese scholars, we extended our search to the China National Knowledge Infrastructure (CNKI), merging the search of Chinese and English papers to obtain a clearer picture of the application of the GOCI. A total of 746 documents were retrieved through CNKI with GOCI as the keyword, of which 323 were classified and analyzed according to the "subject". Figure 7 shows that most research was on "SPM" and "Chla", followed by "Estimation studies" and "Spatial and temporal resolution", which can be seen from the size of the box area.

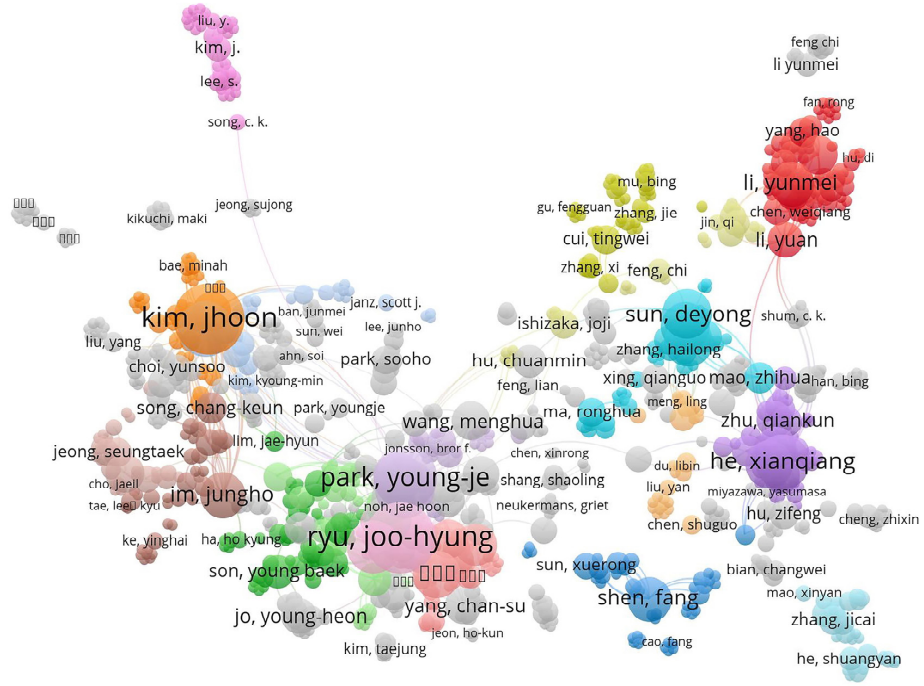

Figure 6. Keyword mapping from the Web of Science, searched by author name.

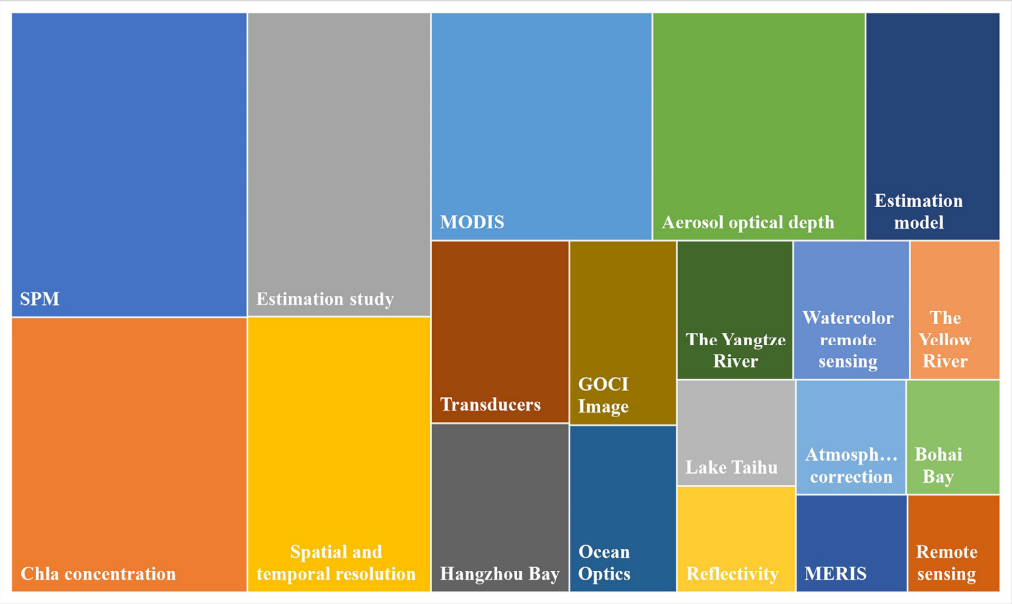

Figure 7. Overview of the application of GOCI retrieved by subject terms from CNKI.

In summary, it can be seen that awareness about GOCI satellites is increasing annually, and their application in various fields is becoming increasingly extensive. In the past decade, the application of the GOCI in ICWs has become more and more comprehensive. We found that the highest number of studies on Chla concentration estimation by scholars was 23 articles, followed by SPM concentration estimation (22) and ABs (17), accounting for 19%, 18%, and 14%, while there were 13 and 10 studies on AC and water clarity, accounting for 11% and 8%, respectively (Figure 8).

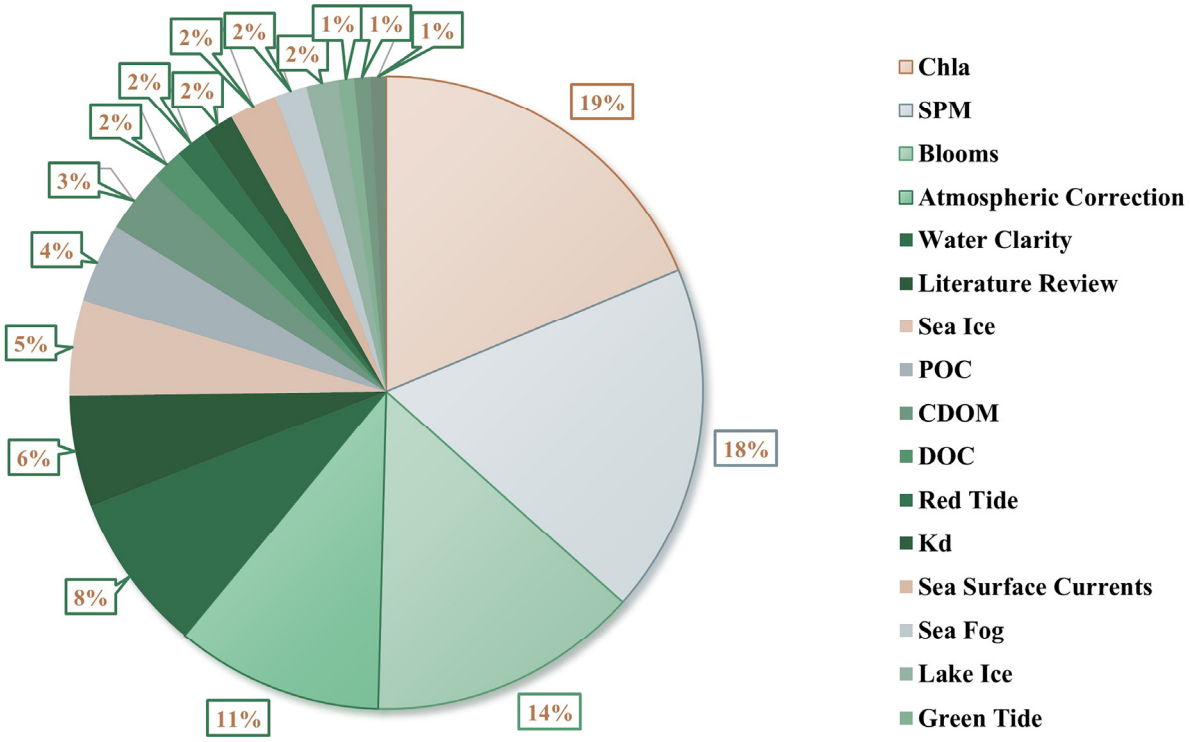

Figure 8. Summary and proportion of the applications of GOCI in inland and coastal waters.

4. Inland and Coastal Waters Monitoring by the GOCI

The GOCI has been entering a rapid development phase in ICW use to offer more services for water quality detection, environmental assessment, and monitoring sudden events. The GOCI will become an important instrument for water color monitoring in the future and will, simultaneously, provide a reference for the design of future water color sensors. In this section, we review the capabilities of the GOCI. We first provide an overview of AC algorithms. We compare the advantages and disadvantages of different methods and their applicability. Secondly, we highlight the research progress of scholars on AB monitoring. Finally, the estimation of water quality parameters is reviewed and divided into four aspects: Chla, SPM, water clarity, and other water quality parameters.

4.1. Atmospheric Correction of GOCI Images

AC is the process of obtaining the reflectance from the top of the atmosphere as observed by satellites. This process is vital because the $R_{rs}(\lambda)$ is the primary input for most water-quality remote sensing algorithms [72–74]. The GOCI Data Processing System (GDPS) is the official data processing software for the GOCI. The standard AC algorithm of the GOCI evolved initially based on the algorithms of the SeaWiFS and MODIS but then expanded and improved according to the characteristics of the GOCI's own instrument design and research fields [70,75–78]. This model followed a regional empirical relationship between the $R_{rs}(660)$ and two NIR bands ($R_{rs}(745)$ and $R_{rs}(865)$) (denoted as SR660). Aerosol properties from neighboring non-turbid waters were also incorporated to finalize the AC process [75]. Ahn [79] improved the SR660 model by introducing two AC models. The first AC model used $R_{rs}(709)$ to replace the $R_{rs}(660)$, taking advantage of the lower contribution of the absorption signal of non-pure water constituents in $R_{rs}(709)$. SR709 has been shown to perform well in waters with only one sediment type. The second AC model used the 620 nm radiation (denoted as SRIOP) to estimate the $R_{rs}(\lambda)$ in the NIR bands. SRIOP showed good performance in waters with a variety of sediment types.

Another software, the SeaWiFS Data Analysis System (SeaDAS), provides an AC module to the GOCI, including the Management Unit of the North Sea Mathematical Models (MUMM) algorithm, which is used to produce $R_{rs}(\lambda)$ products for the turbid Hangzhou Bay and Yellow River Estuary. MUMM assumes that the magnitude of $R_{rs}(\lambda)$ at 745 and 865 nm is dominated by the backscattering of particles. The ratio of $R_{rs}(745)$ and $R_{rs}(865)$ is assumed to be constant. As aerosol types do not usually vary over spatial scales of about 100 km, the ratio of aerosol reflectance in these two bands can also be regarded as a constant. However, this assumption of $R_{rs}(865)/R_{rs}(745)$ is deemed to be invalid for highly turbid waters. Therefore, Ahn [80], Goyens [81], and Jiang [17] used a second-order polynomial relationship to parametrize $R_{rs}(745)$ and $R_{rs}(865)$ for the AC of the GOCI in highly turbid waters.

The Polymer software also offers a GOCI AC module. However, it is seldom used for the GOCI, even though it has been shown to perform well in turbid coastal waters when applied to satellites like MODIS and OLCI. For extremely turbid waters, such as in parts of Changjiang Estuary, Huanghe Estuary, and Hangzhou Bay, where the SPM can be greater than 500 mg L^{-1}, researchers have proposed innovative AC algorithms for the GOCI. Pan [82] proposed an improved GOCI AC algorithm for the Changjiang (Yangtze) estuary and the adjacent coast. This approach, based on a spectral optimization algorithm (ESOA) with a coupled water–atmosphere model, employed the simple semi-empirical radiative transfer (SERT) model to parameterize $R_{rs}(\lambda)$ based on the SPM concentrations and the aerosol models proposed by [56]. SeaDAS was used to calculate the contributions in aerosols, and the genetic algorithm optimized the ESOA AC process. For highly turbid waters, the $R_{rs}(\lambda)$ in the UV band may be much less than $R_{rs}(\lambda)$ in the NIR band, enabling the UV band's use in estimating aerosol scattering. The UV-AC algorithm was applied to the GOCI by using the 412 nm band as the UV band [83]. The retrieved aerosol or apparent optical properties products of other satellite sensors can also be used to help the GOCI obtain the $R_{rs}(\lambda)$ products.

Many researchers have also developed AC methods for the GOCI under non-ideal observation conditions. Men [84] proposed a novel AC algorithm based on deep learning (denoted as DLACC) to improve the quality of $R_{rs}(\lambda)$ data contaminated by cloud edge effects, including stray light, cloud shadows, and cloud adjacent effects. The observation characteristics of GOCI images from morning to evening also determine that many images have a larger solar zenith angle (SZA) (>70°). It has been reported that a high SZA will increase the residual errors in satellite $R_{rs}(\lambda)$ products due to several factors (e.g., high atmospheric multiple scattering effects and underestimation of the Rayleigh scattering contribution). Li [85] proposed a new neural network (NN) AC algorithm for GOCI data with a high SZA that retrieves $R_{rs}(\lambda)$ directly from Rayleigh-corrected radiance ($L_{rc}(\lambda)$). This NN AC algorithm can retrieve $R_{rs}(\lambda)$ in the morning or evening when NIR and KOSC algorithms fail.

4.2. Algal Blooms

ICWs, due to their high population density, are prone to ABs when certain meteorological conditions arise [86–93]. The impact of ABs, such as the reduction in dissolved oxygen and the release of toxins, presents major challenges to aquatic ecosystem management [9,94–96]. Monitoring ABs is essential for improving water quality and the inhabitants' quality of life and reducing unnecessary losses. A variety of strategies have been developed to monitor and understand algal blooms, integrating satellite data, modeling, and machine learning techniques for improved accuracy and efficiency [97].

As presented in Section 4.1, most existing AC algorithms do not apply to the pixels affected by harmful algal blooms (HABs) or red tides [79,98–101]. Kim [102] developed PUK, a red tide quantification algorithm for the GOCI that does not require an independent AC process, incorporating a radiative transfer simulation combined with a machine-learning technique. Other approaches for extracting the red tide area from the GOCI include the linear mixed model (LMM) and the normalized difference vegetation index (NDVI) threshold method [103]. Also, an improved red tide index (RI) was established by Lou [67] using normalized $L_{rc}(\lambda)$ data at 443, 490, and 555 nm to monitor red tide changes dynamically in the East Lake. Additionally, Lee [104] proposed a newly developed normalized red tide index (NRTI) (calculated with Equations (1)–(4)), utilizing a spectroradiometer to observe the spectral characteristics of red tides and seawater in real-time.

$$P555 = R_{rs}555 - \left(R_{rs}660 + \frac{660-555}{660-490}(R_{rs}490 - R_{rs}660)\right) \quad (1)$$

$$P680 = R_{rs}680 - \left(R_{rs}745 + \frac{745-680}{745-660}(R_{rs}660 - R_{rs}745)\right) \quad (2)$$

$$RTI = \frac{P555}{R_{rs}490} \times \frac{P680}{R_{rs}660} \quad (3)$$

$$NRTI = \frac{RTI}{R_{rs}555 - R_{rs}745} \quad (4)$$

Lagrangian particle tracking experiments allow us to understand the paths of floating green algae patches and explain the physical forcing factors that affect the distribution and advection of floating green algae. Using a combination of GOCI data and numerical simulations helped track and monitor extensive areas in the Yellow Sea and East China Sea [105]. Furthermore, Son [106] developed the Index of floating Green Algae for the GOCI (IGAG) (Equation (5)) using multispectral band ratios of three wavelengths (555, 660, and 745 nm) in the Yellow Sea and East China Sea.

$$IGAG = \frac{R(555) + R(660)}{R(745) - R(660)} + \frac{R(745)}{R(660)} \quad (5)$$

A U-net model for the extraction of long-term spatial variations in ABs along the East China Sea was developed using the GOCI and was trained on two different datasets—six-band channels (all visible bands) and RGB-band channels (443, 555, and 680 nm) [107]. Qiu [108] used a Multi-Layer Perceptron (MLP) machine learning algorithm to establish a novel automatic method to continuously monitor ABs in the Yellow Sea. The method consists of two MLP models, which consider both spectral and spatial features of R_{rc} maps. Accuracy assessment and performance comparison showed that the proposed method has the capability to provide highly accurate prediction maps of macroalgal blooms (F1-score approaching 90% or more) with more robustness than the traditional methods. A novel subpixel-level area estimation method for green algae blooms based on spectral unmixing can detect the existence of green algae and determine their proportion in each pixel. A fast endmember extraction method was proposed to calculate the endmember spectral matrix and the abundance map of green algae automatically, which outperformed existing techniques in experiments on GOCI data [109,110]. Qi [111] used an algal index algorithm to quantify equivalent surface algae density (σ, 0–100%) at pixel and synoptic scales from each cloud-free image and offered an analysis of diurnal changing patterns of σ. Ai [112] and Wang [113] used the alternative floating algae index (AFAI) (Equations (6) and (7)), indicated as follows:

$$AFAI = R_{rc}(\lambda_2) - R_{rc}(\lambda_2)' \quad (6)$$

$$R_{rc}(\lambda_2)' = R_{rc}, \lambda_2 + (R_{rc}, \lambda_3 - R_{rc}, \lambda_1) \times \frac{\lambda_{2-}\lambda_1}{\lambda_3 - \lambda_1} \quad (7)$$

where the subscripts refer to bands (λ_1 = 660 nm, λ_2 = 745 nm, and λ_3 = 865 nm). A classification method was then devised to classify the daily change patterns of ABs automatically into four types to monitor the daily dynamics in Lake Taihu. Li [114] used the cyanobacterial bloom intensity (CBI) index (Equation (8)), combined with meteorological factors, water stability, and nutrient factors, to monitor hourly changes in cyanobacterial blooms in Lake Taihu, indicated here:

$$CBI = \sum_{i=1}^{n} (AFAI_i + 0.001) \quad (8)$$

Xue [110] developed a new floating algae cover (FAC) model following a logistic curve and applied it to China's two large shallow eutrophic lakes, Lake Taihu and Lake Chaohu.

4.3. Water Quality Parameters

The estimation of water quality parameters involves the use of R_{rc} and the underwater irradiance ratio to estimate Chla concentration, SPM concentration, and yellow substance content by calculating the absorption coefficient of phytoplankton, the absorption coefficient of yellow substances, the absorption coefficient of non-pigmented SPM, and the backscattering coefficient ($b_{bp}(\lambda)$) of SPM [65,115,116]. Most commonly, empirical or semi-empirical and artificial intelligence models have been used [117–121]. This section mainly introduces Chla in Section 4.3.1, SPM in Section 4.3.2, and water clarity in Section 4.3.3, and then it briefly introduces other water quality parameters such as CDOM, POC, DOC, NPP, SSS, SSCs, sea ice, sea fog, lake ice, and k_d, among others, in Section 4.3.4.

4.3.1. Chla

The concentration of Chla is the most prevalent pigment in algae and relates to phytoplankton biomass [97,122–127]. Chla concentration is a key indicator of water quality and aquatic ecological health [128–130].

The GOCI official process software suggests using the empirical ocean Chla algorithm (OC3G) for the GOCI using the 443, 490, and 555 bands (Equation (9)) [131], as follows:

$$Chla = 10^{f_0 + f_1 * R + f_2 * R^2 + f_3 * R^3 + f_4 * R^4} \quad (9)$$

where R is calculated as

$$R = \frac{Max(R_{rs}(443),\ R_{rs}(490))}{R_{rs}(555)} \quad (10)$$

and the values of f_0, f_1, f_2, and f_3 are 0.0831, −1.9941, 0.5629, 0.2944, and −0.5458, respectively.

Various studies have explored alternative models and algorithms for Chla estimation in ICWs. Hong [94] explored the physical–biological interaction between anticyclonic mesoscale eddies and Chla secondary blooms after spring blooms in the East Sea and Japan Sea using the GOCI OC3G Chla products. Zhao [132] found diurnal changes in GOCI-derived Chla, with generally higher values in the afternoon than in the morning, and identified heterogeneities in the temporal and spatial domains. Sakuno [133] applied the Linear Combination Index (LCI) algorithm to the GOCI to map Chla distribution in Tachibana Bay, Japan, and found OC3G to have relatively large uncertainties in turbid ICWs. Park [129] developed MFNN, a neural algorithm that can classify the pixels of GOCI images into three Chla concentration categories (normal, abnormally high, and abnormally low) so that outliers can be identified and provide quality control of GOCI Chla products.

A spectral index method, such as the fluorescence line height (FLH) [134], helped construct a band conversion relationship from 681 to 685 nm to establish a phytoplankton retrieval model suitable for the GOCI. Wang [68] calibrated three empirical spectral index algorithms (OC4, OC5, and Yellow and East China Sea Ocean Color (YOC)) and constructed four machine learning algorithms (BP neural network (BPNN), random forest (RF), AdaBoost, and support vector regression (SVR)) using numerous in situ data collected in the Bohai Sea and Yellow Sea. The comparison illustrated that machine learning methods were more accurate than classic spectral index algorithms and that RF performed best. The waters in Hangzhou Bay were classified into moderately and extremely turbid based on the ratio of $R_{rs}(745)/R_{rs}(490)$ [135]. Then, the OC3G and modified synthetic chlorophyll index (SCI) index were used for these two water types to map Chla distribution in this bay [135]. Fan [97] modified the generalized algal bloom index algorithm (GABI) to map Chla in the turbid Changjiang Estuary. For this water region, the modified GABI algorithm showed better accuracy and stability than the two-band ratio, as well the three-band, and four-band spectral algorithms.

Lake Taihu is a favorite research area for GOCI Chla model construction and application in inland waters. Bao [136] proposed a weighted algorithm to estimate Chla concentrations based on spectral classification and weighted matching using normalized mutual information (NMI). Huang [137] proposed a regional NIR red ratio algorithm ($R_{rs}(745)/R_{rs}(680)$) for Chla retrieval in Lake Taihu. Based on this model, the hourly Chla maps of Lake Taihu were produced from 6 August to 9 August 2013. In this paper, the GOCI-derived Chla products revealed clear evidence of hourly spatial and temporal variations in Chla in the eutrophic inland waters. The $R_{rs}(745)/R_{rs}(680)$ was also used by Du [115] to analyze the spatio-temporal dynamics of Chla and their response to river flow in the estuary of Lake Taihu. Duan [138] proposed a three-band model using GOCI 681, 745, and 865 nm bands. Guo [139] proposed another three-band Chla model ($R_{rs}^{-1}(681) - R_{rs}^{-1}(709) * R_{rs}(753)$) for the GOCI. Simulated and in situ data illustrated that the three-band model outperformed the two-band model under various SPM conditions. Guo [140] proposed a bio-optical hyperspectral reconstruction (BBHR) algorithm to generate simulated hyperspectral $R_{rs}(\lambda)$ ranging in wavelengths from 400 to 800 nm from the GOCI and five widely used water color sensors. Simulated hyperspectral $R_{rs}(\lambda)$ facilitate the construction of more accurate Chla estimation models for optically complex turbid inland waters. Guo [141] compared the performance of different Chla algorithms for the GOCI and the GOCI-II in Lake Taihu, Lake Chaohu, and Lake Hongze, with $L_{rc}(\lambda)$ as input. The results indicated that the RF algorithm outperformed the commonly used spectral index models.

4.3.2. SPM

SPM refers to the substances suspended in a water body and can be used to characterize its cleanliness [9,142–145]. SPM includes inorganic substances (such as minerals, salts, and metals), particles from algae, silt and clay, and other organic matter [146]. SPM directly affects the propagation of light in the water body, which in turn affects the aquatic ecological environment and ultimately determines the primary productivity of the lake [20,147–149].

The initial GOCI SPM standard product was based on the algorithm proposed by Ahn [150] and Moon [151] as Equation (11), indicated here:

$$SPM = 945.07 * (R_{rs}(555))^{1.137} \tag{11}$$

Ruddick [152] applied the SPM model proposed by Nechad [153] to the GOCI as Equation (12) for comparison with the first official SPM algorithm above, as follows:

$$SPM = A_{745} * \frac{\pi * R_{rs}(745)}{1 - \pi R_{rs}(745)/C_{745}} \tag{12}$$

where A_{745} equals 1755, and C_{745} equals 0.198. This paper found that GOCI data can be used to qualitatively study SPM dynamics except in extremely turbid waters, which are masked out of the GOCI official $R_{rs}(\lambda)$ products. The following standard GOCI SPM was retrieved by the YOC algorithm based on Siswanto's SPM retrieval model for the Yellow and East China Sea (as Equation (13)) [154–156]:

$$SPM = 10^{(0.649+25.623*(R_{rs}(555)+R_{rs}(670))-0.646*(\frac{R_{rs}(490)}{R_{rs}(555)}))} \tag{13}$$

He [83] developed a two-band ratio SPM algorithm ($R_{rs}(745)/(R_{rs}(490))$ for Hangzhou Bay and nearby coastal waters. The diurnal variations derived by the GOCI showed a good relationship with the buoy data in the region. Yu [157] proposed an experiential SPM algorithm suitable for the Bohai Sea and Yellow Sea to evaluate the effects of typhoons on SPM by carrying out parameter optimization and genetic programming, as with Equation (14).

$$\lg(SPM) = 4.8581 + 0.8206 * \frac{R_{rs}(745)}{R_{rs}(490)} - 0.9998 * \frac{R_{rs}(555)}{R_{rs}(490)} - 3.6504 * \sqrt{\frac{R_{rs}(490)}{R_{rs}(555) + R_{rs}(660)}} \tag{14}$$

Also, using this model, Cheng [158] studied dynamic variations in SPM in China's macro-tidal Yalu River estuary. Choi [159] and Meng [160] developed a single-red band model ($R_{rs}(660)$) to retrieve SPM on the west coast of the Korean Peninsula and Bohai Sea. Liu [148] developed an empirical SPM retrieval algorithm based on the spectral absorption index (SAI) in highly turbid Hangzhou Bay with Equations (15) and (16).

$$SAI = \frac{d * R_{rs}(490) + \left(1 - \frac{555-490}{745-490}\right) * R_{rs}(745)}{R_{rs}(555)} \tag{15}$$

$$SPM = 10^{2.01814*SAI+0.83774} \tag{16}$$

Lyu [119] developed a two-step SPM retrieval model using in situ simulated GOCI $R_{rs}(\lambda)$ and SPM data collected in Lake Taihu, Lake Chaohu, Lake Dianchi, and the Three Gorges Reservoir. Firstly, a clustering method was applied to classify the turbid inland waters into three types (Type 1, Type 2, and Type 3). Secondly, the best performing of the three SPM algorithms was gauged and determined via comparison of their results (Type 1: $R_{rs}(865)/R_{rs}(555)$, Type 2: $R_{rs}(745)/R_{rs}(555)$, and Type 3: $R_{rs}(745)/R_{rs}(555)$). Similarly, Huang [137] proposed another classification-based SPM inversion algorithm in Lake Taihu.

The waters were classified into two types based on the $R_{rs-depth}(680)$ index calculated with Equation (17), indicated as follows:

$$R_{rs-depth}(680) = \left\{ R_{rs}(660) + [R_{rs}(745) - R_{rs}(660)] * \frac{745-680}{745-660} \right\} - R_{rs}(680) \quad (17)$$

For the waters with $R_{rs-depth}(680) \leq 0.005$, the two-band ratio (Equation (18)) was used, and for the waters with $R_{rs-depth}(680) > 0.005$, the three-band algorithm (Equation (19)) was used.

$$BR_{SPM} = 10^{2.2135/(1+\exp(-(\frac{R_{rs}(745)}{R_{rs}(555)}-0.1223/0.1439)))} \quad (18)$$

$$TBA_{SPM} = 10^{2.314/(1+\exp(-(\frac{R_{rs}(745)+R_{rs}(680)}{R_{rs}(555)}-0.6263)/0.431))} \quad (19)$$

Du [115] proposed a single NIR band algorithm ($R_{rs}(745)$) to retrieve SPM in the estuary of northwest Lake Taihu. Zhang [161] developed a semi-analytical SPM model for estimating SPM using the satellite in situ matchup data collected in Lake Taihu and Hangzhou Bay. He [162] calibrated the SPM model proposed by He [83] to map SPM products using the GOCI in Lake Taihu as Equation (20).

$$SPM = 10^{0.61+1.43*R_{rs}(745)/R_{rs}(490)} \quad (20)$$

The GOCI-derived SPM products are consistent with a two-dimensional model that couples shallow water and SPM transport dynamics. The high-spatial-resolution GOCI SPM product combined with the hydrodynamic model provides the opportunity to monitor the suspended solids transport with high-time frequency monitoring. Xu [145] developed a quadratic polynomial model of one variable ($R_{rs}(745) + R_{rs}(865)$) to map SPM in Lake Taihu (Equation (21)).

$$SPM = 32,517 * (R_{rs}(745) + R_{rs}(865))^2 + 1327.2 * (R_{rs}(745) + R_{rs}(865)) + 0.5 \quad (21)$$

From the hourly GOCI-derived SPM products, they found that the Tiaoxi River greatly influenced the spatial distributions of SPM in Lake Taihu by the plumes after heavy precipitation events. Lei [147] developed a multivariate linear stepwise regression method for the retrieval of the surface horizontal distribution of SPM using the GOCI. Then, the estimation model of the vertical structure of underwater SPM was constructed using layer-by-layer recursion. These efforts retrieved the horizontal and vertical distribution of SPM concentration from GOCI data over Lake Hongze.

4.3.3. Water Clarity

Water clarity is a critical parameter for the optical properties of ICWs [145,163–166], vital for characterizing the turbidity and absorption/scattering of light by water bodies. It directly relates to the inherent optical properties of waterbodies, such as Chla, SPM, and phytoplankton biomass [167–172].

To estimate water clarity using GOCI data, Zhou [172] proposed a regional linear corrected Secchi disk depth (SDD) model based on the mechanical model developed by Lee [173] (denoted as SDD_{Lee}). This model uses the GOCI $R_{rs}(\lambda)$ derived by the MUMM in Jiaozhou Bay, and its formulation is given in Equation (22) as follows:

$$SDD_{Lee} = \frac{1}{2.5Min(K_d^{tr})} In(\frac{|0.14 - R_{rs}^{tr}|}{0.013}) \quad (22)$$

where $Min(K_d^{tr})$ is the minimum K_d in the visible bands (412, 443, 490, 555, 660, and 680 nm), while R_{rs}^{tr} is the $R_{rs}(\lambda)$ corresponding to the waveband with the minimum K_d value. The model considers factors like SZA, tides, and wind force to control diurnal variations. Liu [174] validated the suitability of SDD_{Lee} using in situ $R_{rs}(\lambda)$ products and SDD in Jiaozhou Bay and Qingdao coastal areas. Liu [175] compared the retrieved SDD

by different atmospheric correction products, and the previous conclusions regarding the hourly variations in biochemical parameters using the GOCI were improved. Ref. [168] found that the retrieved SDD by SDD_{Lee} was underestimated for their in situ data collected in the Bohai Sea and Yellow Sea due to the uncertainties in the estimation of $K_d(490)$ in SDD_{Lee} in turbid waters. They replaced the original $K_d(490)$ estimation method using a weighted $K_d(490)$ proposed by Mao [176] combined with two $K_d(490)$ estimation methods (one for clear and one for turbid water) and a weighted coefficient. Ding [177] used the GOCI-derived Chla and SPM products to calculate $a(\lambda)$ and $b_b(\lambda)$ and then input them into the semi-analytical model proposed by He [178] and He [179] (denoted as SDD_{He}) to retrieve SDD in the eastern Chinese seas with Equation (23).

$$SDD_{He} = \frac{1}{4(a(\lambda)+b_b(\lambda))} In(\frac{\rho_p \alpha \beta (a(\lambda)+b_b(\lambda))}{C_e f b_b(\lambda)}) \quad (23)$$

Many studies have shown that SDD_{Lee} is biased in estimating SDD in inland waters [167,180]. Bai [167] used a linear relationship to correct SDD_{Lee} (denoted as SDD_{Bai}) and applied this algorithm to the GOCI in Lake Taihu with as Equation (24).

$$SDD_{Bai} = 2.68 * \frac{1}{2.5Min(K_d^{tr})} In\left(\frac{|0.14 - R_{rs}^{tr}|}{0.013}\right) + 0.0046 \quad (24)$$

Zeng [181] proposed an improved Quasi-Analytical Algorithm (QAA)-estimated SDD algorithm (denoted as SDD_{Zeng}) for the GOCI using in situ data collected in Lake Taihu, Lake Hongze, Lake Dongting, and Lake Erhai. SDD_{Zeng} firstly estimated $b_b(745)$ using QAA with an assumption of the pure water absorption ($a_w(745)$), which is dominated at this band ($a(745) \approx a_w(745)$). $K_d(745)$ was estimated using Equation (25) as follows:

$$K_d(745) = (1 + 0.0124 * \theta_s) * a_w(745) + 3.16 * (1 - 0.52 * \exp(-10.8 * a_w(745))) * b_b(745) \quad (25)$$

where θ_s represents the SZA. Zeng [181] found that the $Min(K_d^{tr})$ is at 555 nm in Lake Taihu and Lake Hongze. Thus, a linear relationship was built to convert $K_d(745)$ to $K_d(555)$.

$$K_d(555) = 0.99 * K_d(745) - 1.96 \quad (26)$$

The retrieved $K_d(555)$ was used to retrieve SDD using Equation (22).

In this section, we summarized the proposed algorithms of the GOCI by researchers in ICWs classified by different water quality parameters. These algorithms can be classified as empirical algorithms, semi-analytical algorithms, analytical algorithms, and machine learning algorithms. For Chla, the most widely used algorithms include OC3G (official algorithm), LCI, FLH, SCI, CABI, YOC, BPNN, RF, SVR, NMI, and BBHR. For SPM, the main used algorithms are three-band semi-analytical algorithms and empirical band combination algorithms (e.g., SAI). For SDD, the QAA and improved QAA algorithms are the most widely used.

4.3.4. Other Parameters

In addition to the main water quality parameters above, scholars have also conducted research on CDOM, POC, DOC, NPP, SSS, SSCs, sea ice, sea fog, lake ice, k_d, and other parameters. CDOM is the main constituent of dissolved organic matter (DOM) and a key indicator of water quality conditions [182–184]. Based on QAA and QAA_CDOM, Wang [185] developed a new algorithm named QAA_cj to estimate CDOM concentration. The algorithm can easily be applied to high-turbidity coastal waters. A simple approach to estimate the CDOM concentration was also proposed based on the datasets derived from in situ measurements during four cruise surveys over the Bohai Sea and Yellow Sea. Eight band combination forms (using Xi as a delegate, where i denotes the numerical

order of band combination forms), including single bands, band ratios, and other band combinations by $R_{rs}(\lambda)$ were trained to test the correlations with the CDOM concentrations [186]. POC is an essential form of water carbon, taking part in various biogeochemical processes and influencing both organic and inorganic carbon cycles [187–190]. A remote sensing algorithm that can monitor and accurately estimate the changes in POC fluxes in real-time at the Yangtze Estuary hydrological station was established using GOCI satellite data [191,192]. DOC refers to various dissolved organic molecules ubiquitous in aquatic systems. It is a dynamic reduced carbon pool with important ecological and geochemical functions in inland and coastal waters [193,194]. A regional, red–blue ratio algorithm was proposed to estimate Lake Taihu's surface DOC and analyze its spatiotemporal variation characteristics [195]. Accurate assessments of spatial and temporal changes in NPP in the euphotic zone are critical to understanding the role of the ocean in regulating Earth's climate and assessing future fisheries' production, as well as predicting the impacts of ocean warming, hypoxia, and ocean acidification on marine ecosystems [196–198]. Wu [198] used the Adsorption Based Productivity Model (ABPM) to monitor diurnal and daily surface and euphotic-column integrated NPP. Global changes in SSS can simulate the variations in the exchanges between the atmosphere and the ocean surface, as well as the ocean surface and the deep sea. SSS is also involved in the intensification of the global water cycle. For the estimation of SSS, a multi-layer perceptron neural network (MPNN) was employed to train the nonlinear processes of GOCI-II spectral measurements as inputs and the SSS of the Soil Moisture Active Passive (SMAP) satellite as the target [102]. SSCs are one of the most important physical properties in ocean dynamics and are crucial for understanding ocean physical and biogeochemical processes [69,199,200]. A method based on maximum cross-correlation (MCC) was used to derive changes in SSCs in the highly turbid waters of Hangzhou Bay to capture better tidal phase variations [77]. Sea ice monitoring is vital for marine traffic, fisheries, ports, and weather forecasting. A simple method was proposed that exploited the spatial variability of the sea ice surface and applied spatial convolution filtering, in which the center pixel within the window was replaced by the standard deviation of all pixels within the window, effectively separating thin ice area from open water [201]. Also, accurately detecting sea ice thickness (SIT) is crucial for understanding climate change. Gu [202] proposed an SIT inversion method for Liaodong Bay based on Rayleigh scattering corrected reflectance, which has practical advantages in estimation accuracy and spatiotemporal resolution. This method can also be applied to the global ocean. Also, an object-based feature extraction method and an albedo-based thickness inversion model were used for estimating SIA and SIT, respectively, by Yan [203] to reach a better effect. The emergence of sea fog leads to low visibility and seriously threatens the safety of maritime activities. Therefore, monitoring changes in sea fog is particularly important [204]. Jeon [205] proposed a method to identify sea fog based on the convolutional neural network transfer learning model (CNN-TL). Zhou [204] established a sea fog dataset (SFDD) and a dual-branch sea fog detection network (DB-SFNet). Lake ice is one of the essential climate variables of the cryosphere and is closely related to lake environments, ecological regulation, and the safety of human activities [206–208]. Yang [209] used the enhanced spatial and temporal adaptive reflection fusion model (ESTARFM) to merge Landsat and GOCI images and extracted the length and angles of the linear structure to monitor the hourly changes in the surface morphology of Lake Chagan. k_d is an important optical property of water, which describes the penetration of incident solar radiation in the water column. k_d is a quasi-inherent optical property since it depends on the water constituents and the distribution of the ambient light field [210–213]. An improvement of the parameterization equations in the inverse scheme of the 2Seacolor model was used in the Yangtze Estuary to retrieve k_d [214].

5. Discussions

This section discussed the limitations, uncertainties, and future directions of the GOCI and other geostationary ocean color satellites.

5.1. The Limitations and Uncertainties of Current Studies for the GOCI

Most water color sensors (e.g., MODIS, OLCI, MERIS, and VIIRS) observed the surface water on Earth between the local time of 9:30 a.m. and 2:30 p.m. This is the ideal time window for water color satellite observation. GOCI observation images before or after this time window may face many issues. Firstly, ensuring a sufficient signal-to-noise ratio (SNR) is essential for achieving stable and reliable satellite sensor AC and water quality modeling [215,216]. GOCI images observed in the morning and dusk may have an insufficient SNR, especially in winter [217]. In addition to the SNR, higher observation angles can interfere with the GOCI's AC and water quality modeling processes. For the AC, a high sun zenith angle will increase the residual errors in the satellite $R_{rs}(\lambda)$ products by high atmospheric scattering effects and underestimation of the Rayleigh contribution [24,72]. For water quality modeling, high solar zenith angles (for example, greater than 60°) influence the above-water $R_{rs}(\lambda)$ when extrapolated from the in-water remote sensing ratio. It, in turn, impacts the accuracy of downstream water color retrievals [218]. Until now, we have only found a few papers about obtaining reliable GOCI atmospheric correction and water quality parameter products under unsatisfactory observing conditions [85,131,219].

In addition to high observations, many other issues may reduce the image quality of the GOCI. The sun's glint reflectance of the GOCI is reported to be minor, even in summer [75]. However, GOCI observation images may also be affected by the sun glint through the specular reflection phenomenon [220,221]. The satellite observation angles of the GOCI can simply be assumed to be constant. The sun observation angles changed significantly in one day. Under some specific sun, satellite observation angle combination, and water wave conditions, there may be unignorable sun glint reflectance in some observation regions of the GOCI image. The GOCI L2 data have various flags; one is "Bright_Pxl_Adj" (bright pixel adjacency warn) [222]. We are unsure whether it can determine which water pixels are affected by the adjacency effects. There are still too few studies on the impact of adjacency effects on GOCI nearshore water monitoring [56,84,223]. The improved spatial resolution of the GOCI-II (250 m) provides the possibility for monitoring smaller bays, lakes, reservoirs, and rivers. Studying the adjacency effect removal method of the GOCI-II is significant for its application in the areas above.

5.2. Integrating Geostationary Ocean Color Satellites, Unmanned Aerial Vehicles, and Ground Collaborative Observation

Due to cloud interference, it is difficult for the GOCI to take advantage of its high temporal resolution characteristics, especially in cloudy and humid areas [224]. With the development of satellite remote sensing technology, unmanned aerial vehicles and ground observation technology are also growing rapidly, as shown in Figure 9. The development of unmanned aerial vehicles includes improved sensors and payloads, enhanced flight control systems, miniaturization, lightweight design, and higher battery life [225–227]. Ground observation technology progress includes improving sensors and algorithms, providing more accurate estimates of water quality parameters, and the ability to monitor continuously, in the long term, in real time, and automatically [228,229]. The GOCI can be used to produce water quality products in clear weather. In cloudy weather, unmanned aerial vehicle observation results and point ground observation results for an area of interest can be input into hydrodynamic models to generate a simulated numerical water quality dataset [230,231]. The integration of technology can achieve all-weather water quality monitoring of ICWs.

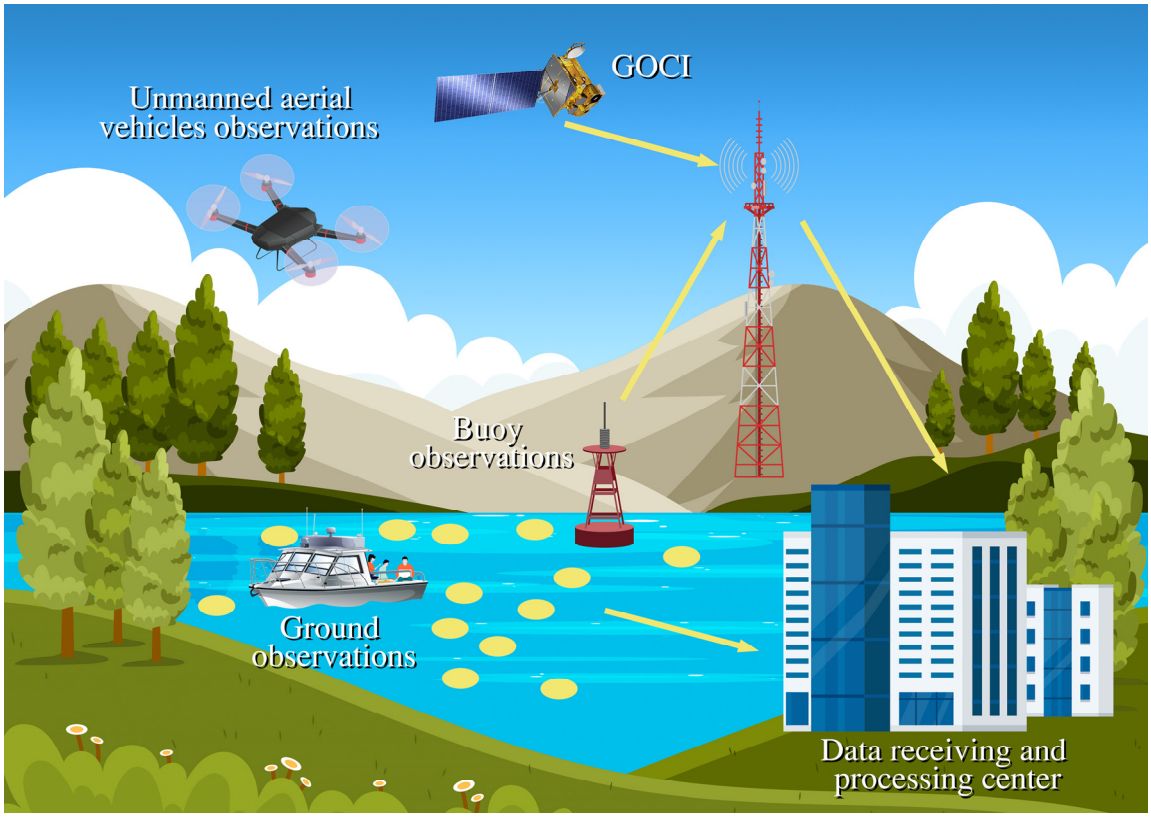

Figure 9. Schematic diagram of integrated ground–air space.

5.3. Fusion of Geostationary Ocean Color Satellites with Other Satellite Products

Image fusion can combine the advantages of different temporal, spatial, and spectral resolution sensors to improve the monitoring of water quality in ICWs [175,232]. Geostationary meteorological satellites (GMSTs) tend to have higher temporal resolution than geostationary ocean color satellites (GOCSs). For example, Himawari 8/9 acquires data every ten minutes, while the GOCI acquires data only once an hour. However, the low signal-to-noise ratio (SNR) and spatial resolution limit the application of GMSTs in water quality monitoring [233]. Taking GOCSs as a reference and fusing them can improve the spatial resolution of GMSTs and enhance spectral information. The fused GMST may produce better water quality products in ICWs than the original images [234]. The schematic diagram of image fusion is shown in Figure 10.

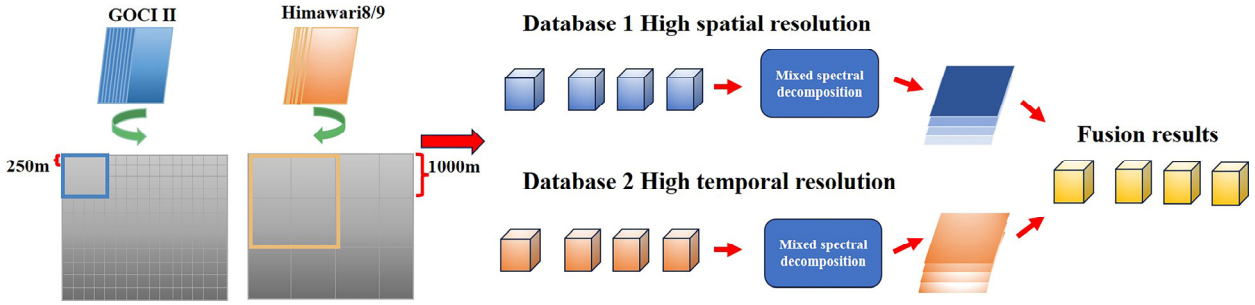

Figure 10. Schematic diagram of image fusion, taking GOCI-II and Himawari8/9 as an example.

Similarly, fusion can also improve GOCS products. The fusion of GOCSs and medium- and high-resolution satellites can improve the spatial resolution of GOCSs, providing more spatial details of ICW quality changes [18]. The fusion of GOCSs and hyperspectral satellites will enhance the spectra of GOCSs, improving the accuracy of the water quality

products of a GOCS [235]. In addition to multiple daily observations, a GOCS, like the GOCI, can provide long-time series observation data. Developing technologies to integrate GOCS products with other long-term series satellite products (SeaWiFS, MODIS, and VIIRS) will contribute to long-term series of water quality assessments [236–239].

5.4. Improving Spectral, Spatial, and Temporal Resolution of Geostationary Ocean Color Sensors

5.4.1. Improving Spectral Resolution

The GOCI was equipped with eight bands (six for visible light and two for NIR). The next generation of the GOCI (GOCI-II) increased the number of bands to thirteen (one for UV, eight for visible, three for near-infrared, and one for broad bandwidth). The new 380 nm ultraviolet band can be used to retrieve parameters related to the absorption of CDOM (e.g., DOC, carbon dioxide, or organic pollutants) [117,240]. It also allows for applying ultraviolet AC methods to the GOCI to provide more reliable $R_{rs}(\lambda)$ products [66,241]. The 510 nm band can potentially improve the performance of OC3G or other blue–green Chla algorithms in relatively clear ICWs [242]. PC can characterize cyanobacterial biomass, which has a distinct absorption peak at about 620 nm [243,244]. Many inland lakes on the Korean Peninsula and East China have frequent occurrences of cyanobacterial blooms [245–248]. The newly added 620 nm band allows the GOCI-II to monitor cyanobacteria blooms quantitatively. The last new band of the GOCI-II is 709 nm. Many studies have illustrated this band's usefulness in Chla retrievals [249,250]. The GOCI-II has the potential to provide more accurate Chla products in turbid ICWs.

The newly added five bands provide many advantages to the GOCI-II compared with the GOCI. The GLIMR is a geostationary sensor funded by the NASA Earth Venture Instrument program, which is anticipated to launch within this decade (around 2026–2027) [62]. The GLIMR is planned to provide 340–1025 nm hyperspectral data of aquatic ecosystems. The hyperspectral characteristic of the GLIMR may provide more reliable atmospherically corrected $R_{rs}(\lambda)$ products and more accurate water quality products (e.g., Chla, SPM, or SDD). By targeting absorption or backscatter characteristics at different wavelengths, the GLIMR may provide more new water quality parameters (e.g., algae species, oil spills, microplastics, or greenhouse gases). The GOCI, GOCI-II, and GLIMR (planned) have only visible and NIR bands. The complex optical properties of ICWs require that $R_{rs}(\lambda)$ products are combined with different AC algorithms based on the bands' wavelengths (e.g., UV, visible, NIR, and SWIR bands) [251]. The next-generation GOCSs should have more band choices.

5.4.2. Improving Spatial Resolution

Most of the applications of the GOCI in inland waters have been carried out in Lake Taihu, Lake Hongze, and Lake Chagan. The coarse spatial resolution of 500 m makes it hard to use the GOCI to monitor water quality in small lakes. With an improved spatial resolution of 250 m, the GOCI-II can monitor more inland waters than the GOCI. Inland lakes with small sizes are more easily affected by human activities and global warming than large lakes [252,253]. A higher spatial resolution allows future GOCSs to monitor the water quality of small and medium-sized lakes.

5.4.3. Improving Temporal Resolution

The most significant advantage of a GOCS is its high temporal resolution. The observation times of GLIMR, the GOCI, and the GOCI-II are six (planned), eight, and ten per day. Many water quality changes, such as AB vertical and horizontal movements [9,254], lacustrine greenhouse gas emission fluxes [255], and estuary sediment fluxes [256,257], tend to happen rapidly, at sub-hourly time scales. We partly summarize and provide some possible future directions for the GOCI and other next-generation GOCSs in this study.

5.5. Further Expansion of GOCI-II Products

Through better spatial and temporal resolution, observation area, optical performance, etc., the GOCI-II has 26 types of official products rather than GOCI 13 types (https://kosc.kiost.ac.kr/index.nm?menuCd=44&lang=en accessed on 20 March 2024). The GOCI-II has the potential to provide more products to help protect the environment of ICWs and coastal areas. The new 380 nm ultraviolet band can be used to retrieve parameters related to the absorption of CDOM, DOC, carbon dioxide, organic pollutants, hypoxia, or oil spills [117,240,258–261]. It also allows for applying ultraviolet AC methods to the GOCI to provide more reliable $R_{rs}(\lambda)$ products [66,241]. The 510 nm band can potentially improve the performance of OC3G or other blue–green Chla algorithms in relatively clear ICWs [242]. PC can characterize a cyanobacterial biomass with a distinct absorption peak at about 620 nm [243,244]. Many inland lakes on the Korean Peninsula and East China have frequent occurrences of cyanobacterial blooms [245–248]. The newly added 620 nm band allows the GOCI-II to monitor cyanobacteria blooms quantitatively. The last new band of the GOCI-II is 709 nm. Many studies have illustrated this band's usefulness in Chla retrievals [249,250]. The GOCI-II has the potential to provide more accurate Chla products in turbid ICWs. As we tested, within one hour of observation, the GOCI-II released the image on its official website for users to download. The quasi-real-time data can be used to monitor many pollution events (e.g., blooms, oil spills, and hypoxia) in the ICWs. In addition to being in the water, the GOCI-II can also monitor intertidal zones where the ocean meets the land between high and low tides [262]. They are home to diverse organisms (e.g., algae, mollusks, crustaceans, fish, and birds) specially adapted to survive in this dynamic environment [263]. These zones experience drastic changes in environmental conditions (e.g., fluctuations in temperature, salinity, and exposure to air and sunlight, depending on the tide cycle) [264]. The higher temporal resolution and improved spatial resolution of the GOCI-II can be used to identify and classify intertidal areas.

6. Conclusions

We reviewed the applications of the GOCI for AC and water quality parameter retrieval in ICWs. First, we introduced the GOCI specifications and compared them with those of other satellites, highlighting the advantages of the GOCI in high-temporal water quality monitoring. Then, AC and water quality (such as ABs, Chla, SPM, SDD, and others) algorithms for the GOCI were systematically introduced. The results of the bibliometric analysis showed that many papers were published in the last thirteen years, starting in 2010.

A number of AC or water quality retrieval models for the GOCI have been proposed over the years. These models form a GOCI algorithm library for monitoring water quality in various ICWs. Due to the complex optical properties of ICWs, it is difficult to identify one best performing model of AC or one specific water quality parameter (ABs, Chla, SPM, SDD, or others), as they differ across ICW waterbodies or even across the seasons in the same waterbody. The GOCI provides valuable experience for effectively using a GOCS to monitor the water qualities of ICWs. So far, there is still no official GOCI product for water quality monitoring in ICWs. Classifying the ICWs into different water types and retrieving the water quality by the most suitable model for each type may provide an official, reliable, and high-accuracy water color product for various ICWs.

We partly summarize and introduce future directions for GOCI technology and other next-generation GOCSs to better serve the water quality monitoring of ICWs. Cloudy weather limits the use of high-temporal GOCS satellites. Integrating GOCSs, unmanned aerial vehicles, and ground collaborative observation can achieve all-weather water quality monitoring of ICWs. A GMST tends to have higher temporal resolution than a GOCS and lower spatial and spectral resolutions. The fusion of GOCSs with other GMSTs will improve the spatial and spectral ability of the GMSTs. The fusion of GOCSs with other high spatial or spectral sensors will enhance the image quality of the GOCS itself to monitor ICWs. We suggest that the next generation of GOCSs improve their spatial, spectral, and temporal resolution to better monitor the water quality of ICWs.

Supplementary Materials: The following supporting information can be downloaded at: https://www.mdpi.com/article/10.3390/rs16091623/s1, Table S1: Abbreviation or symbols; Table S2: The number of articles published based on GOCI in the past ten years, the country, the study area, and research direction.

Author Contributions: Conceptualization: G.L., K.S.; Methodology: S.S., Y.W.; Data curation: S.S., G.L.; Formal analysis: S.S., G.L., Y.W.; Investigation: S.S., Y.W.; Writing—original draft: G.L., K.S.; Writing—review and editing: K.S. All authors have read and agreed to the published version of the manuscript.

Funding: The research was jointly supported by the National Key Research and Development Program of China (2021YFB3901101), the National Natural Science Foundation of China (No. 42171385, U23A2008), the Open Fund of State Laboratory of Information Engineering in Surveying, Mapping and Remote Sensing, Wuhan University (Grant No. 22R02) and the Youth Innovation Promotion Association of Chinese Academy of Sciences, China (2022228).

Data Availability Statement: The GOCI and GOCI-II data that support the findings of this study are openly available at https://oceancolor.gsfc.nasa.gov/cgi/browse.pl?per=MO&day=16892&sub=level3&prm=TC&set=80&ndx=0&mon=16161&sen=goci&rad=0&frc=0&cn=90&cs=-90&cw=-180&ce=180&dnm=D and https://www.nosc.go.kr/eng/program/actionTimeSeries.do accessed on 20 March 2024.

Conflicts of Interest: The authors declare that they have no known competing financial interests or personal relationships that could have appeared to influence the work reported in this paper.

References

1. Schofield, O.; Arnone, R.A.; Bissett, W.P.; Dickey, T.D.; Davis, C.O.; Finkel, Z.; Oliver, M.; Moline, M.A. Watercolors in the coastal zone: What can we see? *Oceanography* **2004**, *17*, 30–37. [CrossRef]
2. Shi, J.; Shen, Q.; Yao, Y.; Zhang, F.; Li, J.; Wang, L. Field Radiometric Calibration of a Micro-Spectrometer Based on Remote Sensing of Plateau Inland Water Colors. *Appl. Sci.* **2023**, *13*, 2117. [CrossRef]
3. Morel, A.; Prieur, L. Analysis of variations in ocean color 1. *Limnol. Oceanogr.* **1977**, *22*, 709–722. [CrossRef]
4. Gordon, H.R.; Morel, A.Y. *Remote Assessment of Ocean Color for Interpretation of Satellite Visible Imagery: A Review*; Springer: Berlin/Heidelberg, Germany, 2012.
5. Sathyendranath, S. Reports of the International Ocean-Colour Coordinating Group. *IOCCG Proj. Off. Dartm. Nova Scotia IOCCG Rep.* **2000**, *3*, 140.
6. Schroeder, T.; Schaale, M.; Fischer, J. Retrieval of atmospheric and oceanic properties from MERIS measurements: A new Case-2 water processor for BEAM. *Int. J. Remote Sens.* **2007**, *28*, 5627–5632. [CrossRef]
7. Kyryliuk, D.; Kratzer, S. Evaluation of Sentinel-3A OLCI products derived using the Case-2 Regional CoastColour processor over the Baltic Sea. *Sensors* **2019**, *19*, 3609. [CrossRef] [PubMed]
8. Ding, X.; He, X.; Bai, Y.; Zhu, Q.; Gong, F.; Li, H.; Li, J. High-frequency and tidal period observations of suspended particulate matter in coastal waters by AHI/Himawari-8. *Opt. Express* **2020**, *28*, 27387–27404. [CrossRef] [PubMed]
9. Li, J.; Li, Y.; Bi, S.; Xu, J.; Guo, F.; Lyu, H.; Dong, X.; Cai, X. Utilization of GOCI data to evaluate the diurnal vertical migration of Microcystis aeruginosa and the underlying driving factors. *J. Environ. Manag.* **2022**, *310*, 114734. [CrossRef]
10. Mouw, C.B.; Greb, S.; Aurin, D.; DiGiacomo, P.M.; Lee, Z.; Twardowski, M.; Binding, C.; Hu, C.; Ma, R.; Moore, T.; et al. Aquatic color radiometry remote sensing of coastal and inland waters: Challenges and recommendations for future satellite missions. *Remote Sens. Environ.* **2015**, *160*, 15–30. [CrossRef]
11. Palmer, S.C.J.; Kutser, T.; Hunter, P.D. Remote sensing of inland waters: Challenges, progress and future directions. *Remote Sens. Environ.* **2015**, *157*, 1–8. [CrossRef]
12. Wang, S.; Zhang, X.; Chen, N.; Tian, L.; Zhang, Y.; Nam, W.H. A systematic review and quantitative meta-analysis of the relationships between driving forces and cyanobacterial blooms at global scale. *Environ. Res.* **2023**, *216*, 114670. [CrossRef] [PubMed]
13. Zeng, F.; Song, C.; Cao, Z.; Xue, K.; Lu, S.; Chen, T.; Liu, K. Monitoring inland water via Sentinel satellite constellation: A review and perspective. *ISPRS J. Photogramm. Remote Sens.* **2023**, *204*, 340–361. [CrossRef]
14. Hovis, W.A.; Clark, D.; Anderson, F.; Austin, R.; Wilson, W.; Baker, E.; Ball, D.; Gordon, H.; Mueller, J.; El-Sayed, S. Nimbus-7 Coastal Zone Color Scanner: System description and initial imagery. *Science* **1980**, *210*, 60–63. [CrossRef] [PubMed]
15. Conkright, M.; Gregg, W. Comparison of global chlorophyll climatologies: In situ, CZCS, Blended in situ-CZCS and SeaWiFS. *Int. J. Remote Sens.* **2003**, *24*, 969–991. [CrossRef]
16. Cracknell, A.P. The development of remote sensing in the last 40 years. *Int. J. Remote Sens.* **2018**, *39*, 8387–8427. [CrossRef]
17. Jiang, L.; Wang, M. Improved near-infrared ocean reflectance correction algorithm for satellite ocean color data processing. *Opt. Express* **2014**, *22*, 21657–21678. [CrossRef]
18. Pan, Y.; Shen, F.; Wei, X. Fusion of Landsat-8/OLI and GOCI Data for Hourly Mapping of Suspended Particulate Matter at High Spatial Resolution: A Case Study in the Yangtze (Changjiang) Estuary. *Remote Sens.* **2018**, *10*, 158. [CrossRef]

19. Salisbury, J.; Davis, C.; Erb, A.; Hu, C.; Gatebe, C.; Jordan, C.; Lee, Z.; Mannino, A.; Mouw, C.; Schaaf, C.; et al. Coastal Observations from a New Vantage Point. *Eos* **2016**, *97*. [CrossRef]
20. Wu, J.; Chen, C.; Nukapothula, S. Atmospheric Correction of GOCI Using Quasi-Synchronous VIIRS Data in Highly Turbid Coastal Waters. *Remote Sens.* **2019**, *12*, 89. [CrossRef]
21. Wang, M.; Shi, W. The NIR-SWIR combined atmospheric correction approach for MODIS ocean color data processing. *Opt. Express* **2007**, *15*, 15722–15733. [CrossRef]
22. Shi, W.; Wang, M. Detection of turbid waters and absorbing aerosols for the MODIS ocean color data processing. *Remote Sens. Environ.* **2007**, *110*, 149–161. [CrossRef]
23. Agarwal, N.; Sharma, R.; Thapliyal, P.; Gangwar, R.; Kumar, P.; Kumar, R. Geostationary satellite-based observations for ocean applications. *Curr. Sci.* **2019**, *117*, 506–515. [CrossRef]
24. Bailey, S.W.; Werdell, P.J. A multi-sensor approach for the on-orbit validation of ocean color satellite data products. *Remote Sens. Environ.* **2006**, *102*, 12–23. [CrossRef]
25. Cao, C.; Wang, S.; Li, J.; Zhao, H.; Shen, W.; Xie, Y. MODIS-based monitoring of spatial distribution of trophic status in 144 key lakes and reservoirs of China in summer of 2018. *J. Lake Sci.* **2021**, *33*, 405–413.
26. He, M.; He, S.; Zhang, X.; Zhou, F.; Li, P. Assessment of Normalized Water-Leaving Radiance Derived from GOCI Using AERONET-OC Data. *Remote Sens.* **2021**, *13*, 1640. [CrossRef]
27. Tan, Z.; Cao, Z.; Shen, M.; Chen, J.; Song, Q.; Duan, H. Remote Estimation of Water Clarity and Suspended Particulate Matter in Qinghai Lake from 2001 to 2020 Using MODIS Images. *Remote Sens.* **2022**, *14*, 3094. [CrossRef]
28. Xiong, J.; Lin, C.; Ma, R.; Cao, Z. Remote Sensing Estimation of Lake Total Phosphorus Concentration Based on MODIS: A Case Study of Lake Hongze. *Remote Sens.* **2019**, *11*, 2068. [CrossRef]
29. Baldwin, D.; Tschudi, M.; Pacifici, F.; Liu, Y. Validation of Suomi-NPP VIIRS sea ice concentration with very high-resolution satellite and airborne camera imagery. *ISPRS J. Photogramm. Remote Sens.* **2017**, *130*, 122–138. [CrossRef]
30. Justice, C.O.; Román, M.O.; Csiszar, I.; Vermote, E.F.; Wolfe, R.E.; Hook, S.J.; Friedl, M.; Wang, Z.; Schaaf, C.B.; Miura, T. Land and cryosphere products from Suomi NPP VIIRS: Overview and status. *J. Geophys. Res. Atmos.* **2013**, *118*, 9753–9765. [CrossRef]
31. Lin, L.; Hao, X.; Zhang, B.; Zou, C.-Z.; Cao, C. Assessment of the Reprocessed Suomi NPP VIIRS Enterprise Cloud Mask Product. *Remote Sens.* **2021**, *13*, 2502. [CrossRef]
32. Wang, M.; Jiang, L. VIIRS-derived ocean color product using the imaging bands. *Remote Sens. Environ.* **2018**, *206*, 275–286. [CrossRef]
33. Park, M.-S.; Lee, S.; Ahn, J.-H.; Lee, S.-J.; Choi, J.-K.; Ryu, J.-H. Decadal measurements of the first Geostationary Ocean Color Satellite (GOCI) compared with MODIS and VIIRS data. *Remote Sens.* **2021**, *14*, 72. [CrossRef]
34. Xia, L.; Mao, K.; Ma, Y.; Zhao, F.; Jiang, L.; Shen, X.; Qin, Z. An algorithm for retrieving land surface temperatures using VIIRS data in combination with multi-sensors. *Sensors* **2014**, *14*, 21385–21408. [CrossRef] [PubMed]
35. Morrison, J.M.; Jeffrey, H.; Gorter, H.; Anderson, P.; Clark, C.; Holmes, A.; Feldman, G.C.; Patt, F.S. SeaHawk: An advanced CubeSat mission for sustained ocean colour monitoring. In Proceedings of the Sensors, Systems, and Next-Generation Satellites XX, Edinburgh, UK, 26–29 September 2016; pp. 309–319.
36. Arino, O.; Gross, D.; Ranera, F.; Leroy, M.; Bicheron, P.; Brockman, C.; Defourny, P.; Vancutsem, C.; Achard, F.; Durieux, L. GlobCover: ESA service for global land cover from MERIS. In Proceedings of the 2007 IEEE International Geoscience and Remote Sensing Symposium, Barcelona, Spain, 23–28 July 2007; pp. 2412–2415.
37. Doerffer, R.; Schiller, H. The MERIS Case 2 water algorithm. *Int. J. Remote Sens.* **2007**, *28*, 517–535. [CrossRef]
38. Rast, M.; Bezy, J.; Bruzzi, S. The ESA Medium Resolution Imaging Spectrometer MERIS a review of the instrument and its mission. *Int. J. Remote Sens.* **1999**, *20*, 1681–1702. [CrossRef]
39. Hammond, M.L.; Henson, S.A.; Lamquin, N.; Clerc, S.; Donlon, C. Assessing the Effect of Tandem Phase Sentinel-3 OLCI Sensor Uncertainty on the Estimation of Potential Ocean Chlorophyll-a Trends. *Remote Sens.* **2020**, *12*, 2522. [CrossRef]
40. Moses, W.J.; Gitelson, A.A.; Berdnikov, S.; Povazhnyy, V. Estimation of chlorophyll-aconcentration in case II waters using MODIS and MERIS data—Successes and challenges. *Environ. Res. Lett.* **2009**, *4*, 045005. [CrossRef]
41. Xu, Y.; He, X.; Bai, Y.; Wang, D.; Zhu, Q.; Ding, X. Evaluation of Remote-Sensing Reflectance Products from Multiple Ocean Color Missions in Highly Turbid Water (Hangzhou Bay). *Remote Sens.* **2021**, *13*, 4267. [CrossRef]
42. Tilstone, G.H.; Pardo, S.; Dall'Olmo, G.; Brewin, R.J.W.; Nencioli, F.; Dessailly, D.; Kwiatkowska, E.; Casal, T.; Donlon, C. Performance of Ocean Colour Chlorophyll a algorithms for Sentinel-3 OLCI, MODIS-Aqua and Suomi-VIIRS in open-ocean waters of the Atlantic. *Remote Sens. Environ.* **2021**, *260*, 112444. [CrossRef]
43. Deuzé, J.; Bréon, F.; Devaux, C.; Goloub, P.; Herman, M.; Lafrance, B.; Maignan, F.; Marchand, A.; Nadal, F.; Perry, G. Remote sensing of aerosols over land surfaces from POLDER-ADEOS-1 polarized measurements. *J. Geophys. Res. Atmos.* **2001**, *106*, 4913–4926. [CrossRef]
44. Leroy, M.; Deuzé, J.; Bréon, F.; Hautecoeur, O.; Herman, M.; Buriez, J.; Tanré, D.; Bouffies, S.; Chazette, P.; Roujean, J.-L. Retrieval of atmospheric properties and surface bidirectional reflectances over land from POLDER/ADEOS. *J. Geophys. Res. Atmos.* **1997**, *102*, 17023–17037. [CrossRef]
45. Shimoda, H. ADEOS overview. *IEEE Trans. Geosci. Remote Sens.* **1999**, *37*, 1465–1471. [CrossRef]

46. Kurihara, Y.; Murakami, H.; Ogata, K.; Kachi, M. A quasi-physical sea surface temperature method for the split-window data from the Second-generation Global Imager (SGLI) onboard the Global Change Observation Mission-Climate (GCOM-C) satellite. *Remote Sens. Environ.* **2021**, *257*, 112347. [CrossRef]
47. Matsuoka, A.; Campbell, J.W.; Hooker, S.B.; Steinmetz, F.; Ogata, K.; Hirata, T.; Higa, H.; Kuwahara, V.S.; Isada, T.; Suzuki, K. Performance of JAXA's SGLI standard ocean color products for oceanic to coastal waters: Chlorophyll a concentration and light absorption coefficients of colored dissolved organic matter. *J. Oceanogr.* **2022**, *78*, 187–208. [CrossRef]
48. Tanaka, K.; Okamura, Y.; Mokuno, M.; Amano, T.; Yoshida, J. First year on-orbit calibration activities of SGLI on GCOM-C satellite. In Proceedings of the Earth Observing Missions and Sensors: Development, Implementation, and Characterization V, Honolulu, HI, USA, 25–26 September 2018; pp. 101–110.
49. Qu, L.; Liu, M.; Guan, L. Simulation of Thermal Infrared Brightness Temperatures from an Ocean Color and Temperature Scanner Onboard a New Generation Chinese Ocean Color Observation Satellite. *Remote Sens.* **2023**, *15*, 5059. [CrossRef]
50. Heales, C.J.; Lloyd, E. Play simulation for children in magnetic resonance imaging. *J. Med. Imaging Radiat. Sci.* **2022**, *53*, 10–16. [CrossRef]
51. Chakraborty, A.; Kumar, R.; Stoffelen, A. Validation of ocean surface winds from the OCEANSAT-2 scatterometer using triple collocation. *Remote Sens. Lett.* **2013**, *4*, 84–93. [CrossRef]
52. Parmar, R.; Arora, R.; Rao, M.V.; Thyagarajan, K. OCEANSAT 2: Mission and its applications. In Proceedings of the GEOSS and Next-Generation Sensors and Missions, Goa, India, 13–14 November 2006; pp. 62–73.
53. Singh, R.; Kumar, P.; Pal, P.K. Assimilation of Oceansat-2-scatterometer-derived surface winds in the weather research and forecasting model. *IEEE Trans. Geosci. Remote Sens.* **2011**, *50*, 1015–1021. [CrossRef]
54. Lee, S.-J.; Lee, D.-E.; Choi, S.-Y.; Kwon, O.-S. OSMI-1 enhances TRAIL-induced apoptosis through ER stress and NF-κB signaling in colon cancer cells. *Int. J. Mol. Sci.* **2021**, *22*, 11073. [CrossRef]
55. Hamacher, K.; Buchkremer, R. Measuring online sensory consumer experience: Introducing the Online Sensory Marketing Index (OSMI) as a structural modeling approach. *J. Theor. Appl. Electron. Commer. Res.* **2022**, *17*, 751–772. [CrossRef]
56. Lamquin, N.; Mazeran, C.; Doxaran, D.; Ryu, J.-H.; Park, Y.-J. Assessment of GOCI radiometric products using MERIS, MODIS and field measurements. *Ocean Sci. J.* **2012**, *47*, 287–311. [CrossRef]
57. Shin, J.; Lee, J.-S.; Jang, L.-H.; Lim, J.; Khim, B.-K.; Jo, Y.-H. Sargassum detection using machine learning models: A case study with the first 6 months of GOCI-II imagery. *Remote Sens.* **2021**, *13*, 4844. [CrossRef]
58. Warren, M.; Quartly, G.D.; Shutler, J.; Miller, P.I.; Yoshikawa, Y. Estimation of ocean surface currents from maximum cross correlation applied to GOCI geostationary satellite remote sensing data over the Tsushima (Korea) Straits. *J. Geophys. Res. Ocean.* **2016**, *121*, 6993–7009. [CrossRef]
59. Paduan, J.D.; Washburn, L. High-frequency radar observations of ocean surface currents. *Annu. Rev. Mar. Sci.* **2013**, *5*, 115–136. [CrossRef] [PubMed]
60. Ruddick, K.; Neukermans, G.; Vanhellemont, Q.; Jolivet, D. Challenges and opportunities for geostationary ocean colour remote sensing of regional seas: A review of recent results. *Remote Sens. Environ.* **2014**, *146*, 63–76. [CrossRef]
61. Ryu, J.-H.; Han, H.-J.; Cho, S.; Park, Y.-J.; Ahn, Y.-H. Overview of geostationary ocean color imager (GOCI) and GOCI data processing system (GDPS). *Ocean Sci. J.* **2012**, *47*, 223–233. [CrossRef]
62. Schaeffer, B.A.; Whitman, P.; Vandermeulen, R.; Hu, C.; Mannino, A.; Salisbury, J.; Efremova, B.; Conmy, R.; Coffer, M.; Salls, W.; et al. Assessing potential of the Geostationary Littoral Imaging and Monitoring Radiometer (GLIMR) for water quality monitoring across the coastal United States. *Mar. Pollut. Bull.* **2023**, *196*, 115558. [CrossRef] [PubMed]
63. Son, S.; Kim, Y.H.; Kwon, J.-I.; Kim, H.-C.; Park, K.-S. Characterization of spatial and temporal variation of suspended sediments in the Yellow and East China Seas using satellite ocean color data. *GIScience Remote Sens.* **2014**, *51*, 212–226. [CrossRef]
64. Duan, H.; Ma, R.; Hu, C. Evaluation of remote sensing algorithms for cyanobacterial pigment retrievals during spring bloom formation in several lakes of East China. *Remote Sens. Environ.* **2012**, *126*, 126–135. [CrossRef]
65. Li, J.; Gao, M.; Feng, L.; Zhao, H.; Shen, Q.; Zhang, F.; Wang, S.; Zhang, B. Estimation of chlorophyll-a concentrations in a highly turbid eutrophic lake using a classification-based MODIS land-band algorithm. *IEEE J. Sel. Top. Appl. Earth Obs. Remote Sens.* **2019**, *12*, 3769–3783. [CrossRef]
66. Liu, H.; He, X.; Li, Q.; Kratzer, S.; Wang, J.; Shi, T.; Hu, Z.; Yang, C.; Hu, S.; Zhou, Q. Estimating ultraviolet reflectance from visible bands in ocean colour remote sensing. *Remote Sens. Environ.* **2021**, *258*, 112404. [CrossRef]
67. Lou, X.; Hu, C. Diurnal changes of a harmful algal bloom in the East China Sea: Observations from GOCI. *Remote Sens. Environ.* **2014**, *140*, 562–572. [CrossRef]
68. Wang, J.; Tang, J.; Wang, W.; Wang, Y.; Wang, Z. Quantitative Retrieval of Chlorophyll-a Concentrations in the Bohai–Yellow Sea Using GOCI Surface Reflectance Products. *Remote Sens.* **2023**, *15*, 5285. [CrossRef]
69. Yang, H.; Choi, J.K.; Park, Y.J.; Han, H.J.; Ryu, J.H. Application of the Geostationary Ocean Color Imager (GOCI) to estimates of ocean surface currents. *J. Geophys. Res. Ocean.* **2014**, *119*, 3988–4000. [CrossRef]
70. Li, G.; Wang, L.; Wang, X.; Wang, X.; Sun, G. Geostationary ocean color imager and application progress. *Mar. Environ. Sci.* **2014**, *33*, 966–971.
71. Yin, W.; Huang, D. Applications of geostationary satellite data in the study of ocean and coastal short-term processes: Two cases in the East China Sea. In *Remote Sensing of Ocean and Coastal Environments*; Elsevier: Amsterdam, The Netherlands, 2021; pp. 139–154.

72. Chen, J.; He, X.; Quan, W.; Ma, L.; Jia, M.; Pan, D. A statistical analysis of residual errors in satellite remote sensing reflectance data from oligotrophic open oceans. *IEEE Trans. Geosci. Remote Sens.* **2021**, *60*, 4203912. [CrossRef]
73. Gong, S.; Huang, J.; Li, Y.; Wang, H. Comparison of atmospheric correction algorithms for TM image in inland waters. *Int. J. Remote Sens.* **2008**, *29*, 2199–2210. [CrossRef]
74. Zeng, Q.; Zhao, Y.; Tian, L.-Q.; Chen, X.-L. Evaluation on the atmospheric correction methods for water color remote sensing by using HJ-1A/1B CCD image-taking Poyang Lake in China as a case. *Spectrosc. Spectr. Anal.* **2013**, *33*, 1320–1326.
75. Ahn, J.-H.; Park, Y.-J.; Ryu, J.-H.; Lee, B.; Oh, I.S. Development of atmospheric correction algorithm for Geostationary Ocean Color Imager (GOCI). *Ocean Sci. J.* **2012**, *47*, 247–259. [CrossRef]
76. Concha, J.; Mannino, A.; Franz, B.; Kim, W. Uncertainties in the Geostationary Ocean Color Imager (GOCI) Remote Sensing Reflectance for Assessing Diurnal Variability of Biogeochemical Processes. *Remote Sens.* **2019**, *11*, 295. [CrossRef]
77. Hu, Y.; Dou, T.; Yang, B. A review of research on retrieving the concentration of suspended particulate matter and chlorophyll-a in lake based on GOCI images. *J. Water Resour. Water Eng.* **2017**, *28*, 26–39.
78. Huang, X.; Zhu, J.; Han, B.; Jamet, C.; Tian, Z.; Zhao, Y.; Li, J.; Li, T. Evaluation of Four Atmospheric Correction Algorithms for GOCI Images over the Yellow Sea. *Remote Sens.* **2019**, *11*, 1631. [CrossRef]
79. Ahn, J.-H.; Park, Y.-J. Estimating Water Reflectance at Near-Infrared Wavelengths for Turbid Water Atmospheric Correction: A Preliminary Study for GOCI-II. *Remote Sens.* **2020**, *12*, 3791. [CrossRef]
80. Ahn, J.H.; Park, Y.J.; Kim, W.; Lee, B.; Oh, I.S. Vicarious calibration of the Geostationary Ocean Color Imager. *Opt. Express* **2015**, *23*, 23236–23258. [CrossRef] [PubMed]
81. Goyens, C.; Jamet, C.; Ruddick, K.G. Spectral relationships for atmospheric correction. II. Improving NASA's standard and MUMM near infra-red modeling schemes. *Opt. Express* **2013**, *21*, 21176–21187. [CrossRef] [PubMed]
82. Pan, Y.; Shen, F.; Verhoef, W. An improved spectral optimization algorithm for atmospheric correction over turbid coastal waters: A case study from the Changjiang (Yangtze) estuary and the adjacent coast. *Remote Sens. Environ.* **2017**, *191*, 197–214. [CrossRef]
83. He, X.; Bai, Y.; Pan, D.; Huang, N.; Dong, X.; Chen, J.; Chen, C.-T.A.; Cui, Q. Using geostationary satellite ocean color data to map the diurnal dynamics of suspended particulate matter in coastal waters. *Remote Sens. Environ.* **2013**, *133*, 225–239. [CrossRef]
84. Men, J.; Feng, L.; Chen, X.; Tian, L. Atmospheric correction under cloud edge effects for Geostationary Ocean Color Imager through deep learning. *ISPRS J. Photogramm. Remote Sens.* **2023**, *201*, 38–53. [CrossRef]
85. Li, H.; He, X.; Bai, Y.; Shanmugam, P.; Park, Y.-J.; Liu, J.; Zhu, Q.; Gong, F.; Wang, D.; Huang, H. Atmospheric correction of geostationary satellite ocean color data under high solar zenith angles in open oceans. *Remote Sens. Environ.* **2020**, *249*, 112022. [CrossRef]
86. An, D.; Yu, D.; Zheng, X.; Zhou, Y.; Meng, L.; Xing, Q. Monitoring the Dissipation of the Floating Green Macroalgae Blooms in the Yellow Sea (2007–2020) on the Basis of Satellite Remote Sensing. *Remote Sens.* **2021**, *13*, 3811. [CrossRef]
87. Bing, Z.; Xiaoli, C.; Sen, W.; Xinxin, Y. Analysis of the Causes of Cyanobacteria Bloom: A Review. *J. Resour. Ecol.* **2020**, *11*, 405–413. [CrossRef]
88. Blondeau-Patissier, D.; Gower, J.F.R.; Dekker, A.G.; Phinn, S.R.; Brando, V.E. A review of ocean color remote sensing methods and statistical techniques for the detection, mapping and analysis of phytoplankton blooms in coastal and open oceans. *Prog. Oceanogr.* **2014**, *123*, 123–144. [CrossRef]
89. Cannizzaro, J.P.; Barnes, B.B.; Hu, C.; Corcoran, A.A.; Hubbard, K.A.; Muhlbach, E.; Sharp, W.C.; Brand, L.E.; Kelble, C.R. Remote detection of cyanobacteria blooms in an optically shallow subtropical lagoonal estuary using MODIS data. *Remote Sens. Environ.* **2019**, *231*, 111227. [CrossRef]
90. Huan, Y.; Sun, D.; Wang, S.; Zhang, H.; Qiu, Z.; Bilal, M.; He, Y. Remote sensing estimation of phytoplankton absorption associated with size classes in coastal waters. *Ecol. Indic.* **2021**, *121*, 107198. [CrossRef]
91. Paerl, H.W.; Xu, H.; McCarthy, M.J.; Zhu, G.; Qin, B.; Li, Y.; Gardner, W.S. Controlling harmful cyanobacterial blooms in a hyper-eutrophic lake (Lake Taihu, China): The need for a dual nutrient (N & P) management strategy. *Water Res.* **2011**, *45*, 1973–1983. [PubMed]
92. Sakib, M.H.; Rashid, A.H.A.; Yang, C.S. Comparing performance of inter-sensor NDVI for the detection of floating macroalgal blooms in the Yellow Sea. *Indian J. Geo Mar. Sci.* **2021**, *50*, 613–619.
93. Sun, X.; Wu, M.; Xing, Q.; Song, X.; Zhao, D.; Han, Q.; Zhang, G. Spatio-temporal patterns of Ulva prolifera blooms and the corresponding influence on chlorophyll-a concentration in the Southern Yellow Sea, China. *Sci. Total Environ.* **2018**, *640–641*, 807–820. [CrossRef]
94. Hong, T.T.M.; Park, Y.-G.; Choi, J.M. Divergence Observation in a Mesoscale Eddy during Chla Bloom Revealed in Submesoscale Satellite Currents. *Remote Sens.* **2023**, *15*, 995. [CrossRef]
95. Noh, J.H.; Kim, W.; Son, S.H.; Ahn, J.H.; Park, Y.J. Remote quantification of Cochlodinium polykrikoides blooms occurring in the East Sea using geostationary ocean color imager (GOCI). *Harmful Algae* **2018**, *73*, 129–137. [CrossRef]
96. Sun, D.; Huan, Y.; Qiu, Z.; Hu, C.; Wang, S.; He, Y. Remote-Sensing Estimation of Phytoplankton Size Classes from GOCI Satellite Measurements in Bohai Sea and Yellow Sea. *J. Geophys. Res. Ocean.* **2017**, *122*, 8309–8325. [CrossRef]
97. Fan, C.; Zhang, Y.; Wang, X. Chlorophyll-a concentration inversion and distribution with GOCI images in the Changjiang Estuary. In Proceedings of the First International Conference on Spatial Atmospheric Marine Environmental Optics (SAME 2023), Shanghai, China, 7–9 April 2023; pp. 201–210.

98. Choi, J.-K.; Min, J.-E.; Noh, J.H.; Han, T.-H.; Yoon, S.; Park, Y.J.; Moon, J.-E.; Ahn, J.-H.; Ahn, S.M.; Park, J.-H. Harmful algal bloom (HAB) in the East Sea identified by the Geostationary Ocean Color Imager (GOCI). *Harmful Algae* **2014**, *39*, 295–302. [CrossRef]
99. Shen, F.; Tang, R.; Sun, X.; Liu, D. Simple methods for satellite identification of algal blooms and species using 10-year time series data from the East China Sea. *Remote Sens. Environ.* **2019**, *235*, 111484. [CrossRef]
100. Xu, M.; Gao, Z.; Liu, C. Detecting harmful algal blooms using Geostationary Ocean Color Imager (GOCI) data in Bohai Sea, China. In Proceedings of the Remote Sensing and Modeling of Ecosystems for Sustainability XII, San Diego, CA, USA, 9–13 August 2015; pp. 203–208.
101. Yimin, L.; Zhenyu, T.; Chen, Y.; Feng, H.; Di, M.; Juhua, L.; Hongtao, D. Extraction of Algal Blooms in Dianchi Lake Based on Multi-Source Satellites Using Machine Learning Algorithms. *Adv. Earth Sci.* **2022**, *37*, 1141.
102. Kim, D.-W.; Kim, S.-H.; Baek, J.-Y.; Lee, J.-S.; Jo, Y.-H. GOCI-II based sea surface salinity estimation using machine learning for the first-year summer. *Int. J. Remote Sens.* **2022**, *43*, 6605–6623. [CrossRef]
103. Cao, H.; Han, L. Hourly remote sensing monitoring of harmful algal blooms (HABs) in Taihu Lake based on GOCI images. *Environ. Sci. Pollut. Res. Int.* **2021**, *28*, 35958–35970. [CrossRef]
104. Lee, M.-S.; Park, K.-A.; Micheli, F. Derivation of Red Tide Index and Density Using Geostationary Ocean Color Imager (GOCI) Data. *Remote Sens.* **2021**, *13*, 298. [CrossRef]
105. Son, Y.B.; Choi, B.-J.; Kim, Y.H.; Park, Y.-G. Tracing floating green algae blooms in the Yellow Sea and the East China Sea using GOCI satellite data and Lagrangian transport simulations. *Remote Sens. Environ.* **2015**, *156*, 21–33. [CrossRef]
106. Son, Y.B.; Min, J.-E.; Ryu, J.-H. Detecting massive green algae (Ulva prolifera) blooms in the Yellow Sea and East China Sea using geostationary ocean color imager (GOCI) data. *Ocean Sci. J.* **2012**, *47*, 359–375. [CrossRef]
107. Feng, C.; Wang, S.; Li, Z. Long-term spatial variation of algal blooms extracted using the U-net model from 10 years of GOCI imagery in the East China Sea. *J. Environ. Manag.* **2022**, *321*, 115966. [CrossRef]
108. Qiu, Z.; Li, Z.; Bilal, M.; Wang, S.; Sun, D.; Chen, Y. Automatic method to monitor floating macroalgae blooms based on multilayer perceptron: Case study of Yellow Sea using GOCI images. *Opt. Express* **2018**, *26*, 26810–26829. [CrossRef]
109. Pan, B.; Shi, Z.; An, Z.; Jiang, Z.; Ma, Y. A novel spectral-unmixing-based green algae area estimation method for GOCI data. *IEEE J. Sel. Top. Appl. Earth Obs. Remote Sens.* **2016**, *10*, 437–449. [CrossRef]
110. Xue, K.; Ma, R.; Cao, Z.; Shen, M.; Hu, M.; Xiong, J. Monitoring fractional floating algae cover over eutrophic lakes using multisensor satellite images: MODIS, VIIRS, GOCI, and OLCI. *IEEE Trans. Geosci. Remote Sens.* **2022**, *60*, 4211715. [CrossRef]
111. Qi, L.; Hu, C.; Visser, P.M.; Ma, R. Diurnal changes of cyanobacteria blooms in Taihu Lake as derived from GOCI observations. *Limnol. Oceanogr.* **2018**, *63*, 1711–1726. [CrossRef]
112. Ai, Y.; Lee, S.; Lee, J. Drinking water treatment residuals from cyanobacteria bloom-affected areas: Investigation of potential impact on agricultural land application. *Sci. Total Environ.* **2020**, *706*, 135756. [CrossRef] [PubMed]
113. Wang, S.; Zhang, X.; Chen, N.; Wang, W. Classifying diurnal changes of cyanobacterial blooms in Lake Taihu to identify hot patterns, seasons and hotspots based on hourly GOCI observations. *J. Environ. Manag.* **2022**, *310*, 114782. [CrossRef] [PubMed]
114. Li, J.; Li, Y.; Dong, X.; Wang, H.; Cai, X.; Zhu, Y.; Lyu, H.; Zeng, S.; Bi, S.; Wang, G. Contributions of meteorology and nutrient to the surface cyanobacterial blooms at different timescales in the shallow eutrophic Lake Taihu. *Sci. Total Environ.* **2023**, *894*, 165064. [CrossRef] [PubMed]
115. Du, C.; Li, Y.; Wang, Q.; Liu, G.; Zheng, Z.; Mu, M.; Li, Y. Tempo-spatial dynamics of water quality and its response to river flow in estuary of Taihu Lake based on GOCI imagery. *Environ. Sci. Pollut. Res. Int.* **2017**, *24*, 28079–28101. [CrossRef]
116. Wang, M.; Son, S.; Harding, L.W. Retrieval of diffuse attenuation coefficient in the Chesapeake Bay and turbid ocean regions for satellite ocean color applications. *J. Geophys. Res. Ocean.* **2009**, *114*, C10011. [CrossRef]
117. Li, J.; Yu, Q.; Tian, Y.Q.; Becker, B.L. Remote sensing estimation of colored dissolved organic matter (CDOM) in optically shallow waters. *ISPRS J. Photogramm. Remote Sens.* **2017**, *128*, 98–110. [CrossRef]
118. Lin, S.; Jing, C.; Rui, L. A method of water quality analysis: Chlorophyll a concentration estimation of Dongping Lake based on GOCI image. *Environ. Prot.* **2017**, *45*, 60–63.
119. Lyu, H.; Zhang, J.; Zha, G.; Wang, Q.; Li, Y. Developing a two-step retrieval method for estimating total suspended solid concentration in Chinese turbid inland lakes using Geostationary Ocean Colour Imager (GOCI) imagery. *Int. J. Remote Sens.* **2015**, *36*, 1385–1405. [CrossRef]
120. Sagan, V.; Peterson, K.T.; Maimaitijiang, M.; Sidike, P.; Sloan, J.; Greeling, B.A.; Maalouf, S.; Adams, C. Monitoring inland water quality using remote sensing: Potential and limitations of spectral indices, bio-optical simulations, machine learning, and cloud computing. *Earth-Sci. Rev.* **2020**, *205*, 103187. [CrossRef]
121. Qing, S.; Cui, T.; Lai, Q.; Bao, Y.; Diao, R.; Yue, Y.; Hao, Y. Improving remote sensing retrieval of water clarity in complex coastal and inland waters with modified absorption estimation and optical water classification using Sentinel-2 MSI. *Int. J. Appl. Earth Obs. Geoinf.* **2021**, *102*, 102377. [CrossRef]
122. Bao, Y.; Tian, Q.; Chen, M.; Lü, C. Analysis on Diurnal Variation of Chlorophyll-a Concentration of Taihu Lake Based on Optical Classification with GOCI Data. *Guang Pu Xue Yu Guang Pu Fen Xi = Guang Pu* **2016**, *36*, 2562–2567. [PubMed]
123. Cui, T.W.; Zhang, J.; Wang, K.; Wei, J.W.; Mu, B.; Ma, Y.; Zhu, J.H.; Liu, R.J.; Chen, X.Y. Remote sensing of chlorophyll a concentration in turbid coastal waters based on a global optical water classification system. *ISPRS J. Photogramm. Remote Sens.* **2020**, *163*, 187–201. [CrossRef]

124. Hu, M.; Zhang, Y.; Ma, R.; Xue, K.; Cao, Z.; Chu, Q.; Jing, Y. Optimized remote sensing estimation of the lake algal biomass by considering the vertically heterogeneous chlorophyll distribution: Study case in Lake Chaohu of China. *Sci. Total Environ.* **2021**, *771*, 144811. [CrossRef] [PubMed]
125. Kim, W.; Moon, J.-E.; Park, Y.-J.; Ishizaka, J. Evaluation of chlorophyll retrievals from Geostationary Ocean Color Imager (GOCI) for the North-East Asian region. *Remote Sens. Environ.* **2016**, *184*, 482–495. [CrossRef]
126. Neil, C.; Spyrakos, E.; Hunter, P.D.; Tyler, A.N. A global approach for chlorophyll-a retrieval across optically complex inland waters based on optical water types. *Remote Sens. Environ.* **2019**, *229*, 159–178. [CrossRef]
127. Soomets, T.; Toming, K.; Paavel, B.; Kutser, T. Evaluation of remote sensing and modeled chlorophyll-a products of the Baltic Sea. *J. Appl. Remote Sens.* **2022**, *16*, 046516. [CrossRef]
128. Cao, Z.; Wang, M.; Ma, R.; Zhang, Y.; Duan, H.; Jiang, L.; Xue, K.; Xiong, J.; Hu, M. A decade-long chlorophyll-a data record in lakes across China from VIIRS observations. *Remote Sens. Environ.* **2024**, *301*, 113953. [CrossRef]
129. Park, J.-E.; Park, K.-A. Application of Deep Learning for Speckle Removal in GOCI Chlorophyll-a Concentration Images (2012–2017). *Remote Sens.* **2021**, *13*, 585. [CrossRef]
130. Shi, K.; Li, Y.; Li, L.; Lu, H.; Song, K.; Liu, Z.; Xu, Y.; Li, Z. Remote chlorophyll-a estimates for inland waters based on a cluster-based classification. *Sci. Total Environ.* **2013**, *444*, 1–15. [CrossRef] [PubMed]
131. Li, H.; He, X.; Bai, Y.; Chen, X.; Gong, F.; Zhu, Q.; Hu, Z. Assessment of satellite-based chlorophyll-a retrieval algorithms for high solar zenith angle conditions. *J. Appl. Remote Sens.* **2017**, *11*, 012004. [CrossRef]
132. Zhao, D.; Feng, L. Assessment of the Number of Valid Observations and Diurnal Changes in Chl-a for GOCI: Highlights for Geostationary Ocean Color Missions. *Sensors* **2020**, *20*, 3377. [CrossRef] [PubMed]
133. Sakuno, Y.; Makio, K.; Koike, K. Chlorophyll-a Estimation in Tachibana Bay by Data Fusion of GOCI and MODIS Using Linear Combination Index Algorithm. *Adv. Remote Sens.* **2013**, *2013*, 40465. [CrossRef]
134. Zhao, M.; Bai, Y.; Li, H.; He, X.; Gong, F.; Li, T. Fluorescence Line Height Extraction Algorithm for the Geostationary Ocean Color Imager. *Remote Sens.* **2022**, *14*, 2511. [CrossRef]
135. Yang, Y.; He, S.; Gu, Y.; Zhu, C.; Wang, L.; Ma, X.; Li, P. Retrieval of Chlorophyll a Concentration Using GOCI Data in Sediment-Laden Turbid Waters of Hangzhou Bay and Adjacent Coastal Waters. *J. Mar. Sci. Eng.* **2023**, *11*, 1098. [CrossRef]
136. Bao, Y.; Tian, Q.; Chen, M. A Weighted Algorithm Based on Normalized Mutual Information for Estimating the Chlorophyll-a Concentration in Inland Waters Using Geostationary Ocean Color Imager (GOCI) Data. *Remote Sens.* **2015**, *7*, 11731–11752. [CrossRef]
137. Huang, C.; Shi, K.; Yang, H.; Li, Y.; Zhu, A.-X.; Sun, D.; Xu, L.; Zou, J.; Chen, X. Satellite observation of hourly dynamic characteristics of algae with Geostationary Ocean Color Imager (GOCI) data in Lake Taihu. *Remote Sens. Environ.* **2015**, *159*, 278–287. [CrossRef]
138. Duan, H.; Ma, R.; Zhang, Y.; Loiselle, S.A.; Xu, J.; Zhao, C.; Zhou, L.; Shang, L. A new three-band algorithm for estimating chlorophyll concentrations in turbid inland lakes. *Environ. Res. Lett.* **2010**, *5*, 044009. [CrossRef]
139. Guo, Y.; Huang, C.; Li, Y.; Du, C.; Li, Y.; Chen, W.; Shi, L.; Ji, G. an expanded three band model to monitor inland optically complex water using Geostationary Ocean Color Imager (GOCI). *Front. Remote Sens.* **2022**, *3*, 803884. [CrossRef]
140. Yulong, G.; Changchun, H.; Yunmei, L.; Chenggong, D.; Lingfei, S.; Yuan, L.; Weiqiang, C.; Hejie, W.; Enxiang, C.; Guangxing, J. Hyperspectral reconstruction method for optically complex inland waters based on bio-optical model and sparse representing. *Remote Sens. Environ.* **2022**, *276*, 113045. [CrossRef]
141. Guo, Y.; Wei, X.; Huang, Z.; Li, H.; Ma, R.; Cao, Z.; Shen, M.; Xue, K. Retrievals of Chlorophyll-a from GOCI and GOCI-II Data in Optically Complex Lakes. *Remote Sens.* **2023**, *15*, 4886. [CrossRef]
142. Binding, C.E.; Bowers, D.G.; Mitchelson-Jacob, E.G. Estimating suspended sediment concentrations from ocean colour measurements in moderately turbid waters; the impact of variable particle scattering properties. *Remote Sens. Environ.* **2005**, *94*, 373–383. [CrossRef]
143. Cao, Z.; Ma, R.; Duan, H.; Xue, K.; Shen, M. Effect of Satellite Temporal Resolution on Long-Term Suspended Particulate Matter in Inland Lakes. *Remote Sens.* **2019**, *11*, 2785. [CrossRef]
144. Kang, Y.; Dong, C. Spatio-temporal Analysis of suspended sediment Concentration in the Yongjiang Estuary Based on GOCI. *IOP Conf. Ser. Earth Environ. Sci.* **2018**, *108*, 032017. [CrossRef]
145. Xu, Y.; Qin, B.; Zhu, G.; Zhang, Y.; Shi, K.; Li, Y.; Shi, Y.; Chen, L. High Temporal Resolution Monitoring of Suspended Matter Changes from GOCI Measurements in Lake Taihu. *Remote Sens.* **2019**, *11*, 985. [CrossRef]
146. Jiang, D.; Zhang, H.; Zou, T.; Li, Y.; Tang, C.; Li, R. Suspended particle size retrieval based on geostationary ocean color imager (GOCI) in the Bohai Sea. *J. Coast. Res.* **2016**, *74*, 117–125. [CrossRef]
147. Lei, S.; Xu, J.; Li, Y.; Du, C.; Liu, G.; Zheng, Z.; Xu, Y.; Lyu, H.; Mu, M.; Miao, S.; et al. An approach for retrieval of horizontal and vertical distribution of total suspended matter concentration from GOCI data over Lake Hongze. *Sci. Total Environ.* **2020**, *700*, 134524. [CrossRef]
148. Liu, J.; Liu, J.; He, X.; Chen, T.; Zhu, F.; Wang, Y.; Hao, Z.; Chen, P. Retrieval of total suspended particulate matter in highly turbid Hangzhou Bay waters based on geostationary ocean color imager. In Proceedings of the Remote Sensing of the Ocean, Sea Ice, Coastal Waters, and Large Water Regions 2017, Warsaw, Poland, 11–14 September 2017; pp. 105–111.
149. Padial, A.A.; Thomaz, S.M. Prediction of the light attenuation coefficient through the Secchi disk depth: Empirical modeling in two large Neotropical ecosystems. *Limnology* **2008**, *9*, 143–151. [CrossRef]

150. Ahn, Y.-H.; Moon, J.-E.; Gallegos, S. Development of suspended particulate matter algorithms for ocean color remote sensing. *Korean J. Remote Sens.* **2001**, *17*, 285–295.
151. Moon, J.-E.; Ahn, Y.-H.; Ryu, J.-H.; Shanmugam, P. Development of ocean environmental algorithms for Geostationary Ocean Color Imager (GOCI). *Korean J. Remote Sens.* **2010**, *26*, 189–207.
152. Ruddick, K.; Vanhellemont, Q.; Yan, J.; Neukermans, G.; Wei, G.; Shang, S. Variability of suspended particulate matter in the Bohai Sea from the geostationary Ocean Color Imager (GOCI). *Ocean Sci. J.* **2012**, *47*, 331–345. [CrossRef]
153. Nechad, B.; Ruddick, K.G.; Park, Y. Calibration and validation of a generic multisensor algorithm for mapping of total suspended matter in turbid waters. *Remote Sens. Environ.* **2010**, *114*, 854–866. [CrossRef]
154. Hu, Z.; Pan, D.; He, X.; Bai, Y. Diurnal Variability of Turbidity Fronts Observed by Geostationary Satellite Ocean Color Remote Sensing. *Remote Sens.* **2016**, *8*, 147. [CrossRef]
155. Moon, J.-E.; Park, Y.-J.; Ryu, J.-H.; Choi, J.-K.; Ahn, J.-H.; Min, J.-E.; Son, Y.-B.; Lee, S.-J.; Han, H.-J.; Ahn, Y.-H. Initial validation of GOCI water products against in situ data collected around Korean peninsula for 2010–2011. *Ocean Sci. J.* **2012**, *47*, 261–277. [CrossRef]
156. Siswanto, E.; Tang, J.; Yamaguchi, H.; Ahn, Y.-H.; Ishizaka, J.; Yoo, S.; Kim, S.-W.; Kiyomoto, Y.; Yamada, K.; Chiang, C. Empirical ocean-color algorithms to retrieve chlorophyll-a, total suspended matter, and colored dissolved organic matter absorption coefficient in the Yellow and East China Seas. *J. Oceanogr.* **2011**, *67*, 627–650. [CrossRef]
157. Yu, X. *Retrieval of Suspended Matter Concentration and Reconstruction of Missing Data Based on GOCI in Bohai and Yellow Sea*; Ocean University of China: Qingdao, China, 2013.
158. Cheng, Z.; Wang, X.H.; Paull, D.; Gao, J. Application of the geostationary ocean color imager to mapping the diurnal and seasonal variability of surface suspended matter in a macro-tidal estuary. *Remote Sens.* **2016**, *8*, 244. [CrossRef]
159. Choi, J.-K.; Park, Y.J.; Lee, B.R.; Eom, J.; Moon, J.-E.; Ryu, J.-H. Application of the Geostationary Ocean Color Imager (GOCI) to mapping the temporal dynamics of coastal water turbidity. *Remote Sens. Environ.* **2014**, *146*, 24–35. [CrossRef]
160. Meng, Q.; Xu, J.; Wang, L.; Chen, Y.; Wang, X. Diurnal Changes Monitoring and Analysis of the Total Suspended Matters in Bohai Sea Using Geostationary Ocean Color Imager. *IOP Conf. Ser. Earth Environ. Sci.* **2019**, *234*, 012036. [CrossRef]
161. Zhang, M.; Tang, J.; Dong, Q.; Song, Q.; Ding, J. Retrieval of total suspended matter concentration in the Yellow and East China Seas from MODIS imagery. *Remote Sens. Environ.* **2010**, *114*, 392–403. [CrossRef]
162. He, A.; He, X.; Bai, Y.; Zhu, Q.; Gong, F.; Huang, H.; Pan, D. Simulation of Sedimentation in Lake Taihu with Geostationary Satellite Ocean Color Data. *Remote Sens.* **2019**, *11*, 379. [CrossRef]
163. Amin, R.; Shulman, I. Hourly turbidity monitoring using Geostationary Ocean Color Imager fluorescence bands. *J. Appl. Remote Sens.* **2015**, *9*, 096024. [CrossRef]
164. Kukushkin, A.S. Long-term seasonal variability of water transparency in the surface layer of the deep part of the Black Sea. *Russ. Meteorol. Hydrol.* **2014**, *39*, 178–186. [CrossRef]
165. Wang, S.; Mao, Y.; Zheng, L.; Qiu, Z.; Bilal, M.; Sun, D. Remote sensing of water turbidity in the eastern China seas from geostationary ocean colour imager. *Int. J. Remote Sens.* **2020**, *41*, 4080–4101. [CrossRef]
166. Yan, Z.; Dingfeng, Y.; Xiaoyan, L.; Qian, Y.; Yingying, G. Research on remote sensing retrieval and diurnal variation of Secchi disk, depth of Jiaozhou Bay based on GOCI. *Remote Sens. Nat. Resour.* **2021**, *33*, 108.
167. Bai, S.; Gao, J.; Sun, D.; Tian, M. Monitoring Water Transparency in Shallow and Eutrophic Lake Waters Based on GOCI Observations. *Remote Sens.* **2020**, *12*, 163. [CrossRef]
168. Mao, Y.; Wang, S.; Qiu, Z.; Sun, D.; Bilal, M. Variations of transparency derived from GOCI in the Bohai Sea and the Yellow Sea. *Opt. Express* **2018**, *26*, 12191–12209. [CrossRef] [PubMed]
169. Swift, T.J.; Perez-Losada, J.; Schladow, S.G.; Reuter, J.E.; Jassby, A.D.; Goldman, C.R. Water clarity modeling in Lake Tahoe: Linking suspended matter characteristics to Secchi depth. *Aquat. Sci.* **2006**, *68*, 1–15. [CrossRef]
170. Swan, B.K.; Reifel, K.M.; Tiffany, M.A.; Watts, J.M.; Hurlbert, S.H. Spatial and temporal patterns of transparency and light attenuation in the Salton Sea, California, 1997–1999. *Lake Reserv. Manag.* **2007**, *23*, 653–662. [CrossRef]
171. Testa, J.M.; Lyubchich, V.; Zhang, Q. Patterns and Trends in Secchi Disk Depth over Three Decades in the Chesapeake Bay Estuarine Complex. *Estuaries Coasts* **2019**, *42*, 927–943. [CrossRef]
172. Zhou, Y.; Yu, D.; Cheng, W.; Gai, Y.; Yao, H.; Yang, L.; Pan, S. Monitoring multi-temporal and spatial variations of water transparency in the Jiaozhou Bay using GOCI data. *Mar. Pollut. Bull.* **2022**, *180*, 113815. [CrossRef]
173. Lee, Z.; Shang, S.; Hu, C.; Du, K.; Weidemann, A.; Hou, W.; Lin, J.; Lin, G. Secchi disk depth: A new theory and mechanistic model for underwater visibility. *Remote Sens. Environ.* **2015**, *169*, 139–149. [CrossRef]
174. Liu, X.-Y.; Hu, J.-W.; Tian, L.; Yu, D.-F.; Gao, H.; Yang, L.; An, D.-Y. Comparative study on transparency retrieved from GOCI under four different atmospheric correction algorithms in Jiaozhou Bay and Qingdao Coastal area. *IEEE J. Sel. Top. Appl. Earth Obs. Remote Sens.* **2023**, *17*, 2077–2089. [CrossRef]
175. Liu, X.; Wang, M. Global daily gap-free ocean color products from multi-satellite measurements. *Int. J. Appl. Earth Obs. Geoinf.* **2022**, *108*, 102714. [CrossRef]
176. Mao, Y.; Qiu, Z.; Sun, D.; Wang, S.; Lu, Y.; Wu, C.; Yue, X.; Ye, Z. A Novel Remote Sensing Algorithm for Estimating Diffuse Attenuation Coefficient in the BohaiSea and Yellow Sea. *Guangxi Sci.* **2016**, *23*, 513–519.
177. Ding, X.; Gong, F.; Zhu, Q.; Li, J.; Wang, X.; Bai, R.; Xu, Y. Using geostationary satellite ocean color data and superpixel to map the diurnal dynamics of water transparency in the eastern China seas. *Ecol. Indic.* **2022**, *142*, 109219. [CrossRef]

178. He, X.; Pan, D.; Mao, Z. Water-transparency (Secchi Depth) monitoring in the China Sea with the SeaWiFS satellite sensor. In Proceedings of the Remote Sensing for Agriculture, Ecosystems, and Hydrology VI, Maspalomas, Spain, 13–16 September 2004; pp. 112–122.
179. He, X.; Pan, D.; Bai, Y.; Wang, T.; Chen, C.-T.A.; Zhu, Q.; Hao, Z.; Gong, F. Recent changes of global ocean transparency observed by SeaWiFS. *Cont. Shelf Res.* **2017**, *143*, 159–166. [CrossRef]
180. Feng, L.; Hou, X.; Zheng, Y. Monitoring and understanding the water transparency changes of fifty large lakes on the Yangtze Plain based on long-term MODIS observations. *Remote Sens. Environ.* **2019**, *221*, 675–686. [CrossRef]
181. Zeng, S.; Lei, S.; Li, Y.; Lyu, H.; Xu, J.; Dong, X.; Wang, R.; Yang, Z.; Li, J. Retrieval of Secchi Disk Depth in Turbid Lakes from GOCI Based on a New Semi-Analytical Algorithm. *Remote Sens.* **2020**, *12*, 1516. [CrossRef]
182. Battin, T.J.; Luyssaert, S.; Kaplan, L.A.; Aufdenkampe, A.K.; Richter, A.; Tranvik, L.J. The boundless carbon cycle. *Nat. Geosci.* **2009**, *2*, 598–600. [CrossRef]
183. Berggren, M.; Laudon, H.; Jansson, M. Landscape regulation of bacterial growth efficiency in boreal freshwaters. *Glob. Biogeochem. Cycles* **2007**, *21*, GB4002. [CrossRef]
184. Min, S.-H.; Park, M.-O.; Kim, S.-W.; Han, I.-S.; Kim, W.; Park, Y.-J. Correlation between SST and CDOM during Summer Coastal Upwelling along the Southeast Coast of Korea. *J. Coast. Res.* **2018**, *85*, 1471–1475. [CrossRef]
185. Wang, Y.; Shen, F.; Sokoletsky, L.; Sun, X. Validation and Calibration of QAA Algorithm for CDOM Absorption Retrieval in the Changjiang (Yangtze) Estuarine and Coastal Waters. *Remote Sens.* **2017**, *9*, 1192. [CrossRef]
186. Ling, Z.; Sun, D.; Wang, S.; Qiu, Z.; Huan, Y.; Mao, Z.; He, Y. Remote sensing estimation of colored dissolved organic matter (CDOM) from GOCI measurements in the Bohai Sea and Yellow Sea. *Environ. Sci. Pollut. Res. Int.* **2020**, *27*, 6872–6885. [CrossRef] [PubMed]
187. Bai, Y.; Cai, W.J.; He, X.; Zhai, W.; Pan, D.; Dai, M.; Yu, P. A mechanistic semi-analytical method for remotely sensing sea surface pCO2 in river-dominated coastal oceans: A case study from the East China Sea. *J. Geophys. Res. Ocean.* **2015**, *120*, 2331–2349. [CrossRef]
188. Bauer, J.E.; Cai, W.-J.; Raymond, P.A.; Bianchi, T.S.; Hopkinson, C.S.; Regnier, P.A. The changing carbon cycle of the coastal ocean. *Nature* **2013**, *504*, 61–70. [CrossRef] [PubMed]
189. Liu, D.; Bai, Y.; He, X.; Tao, B.; Pan, D.; Chen, C.-T.A.; Zhang, L.; Xu, Y.; Gong, C. Satellite estimation of particulate organic carbon flux from Changjiang River to the estuary. *Remote Sens. Environ.* **2019**, *223*, 307–319. [CrossRef]
190. Regnier, P.; Friedlingstein, P.; Ciais, P.; Mackenzie, F.T.; Gruber, N.; Janssens, I.A.; Laruelle, G.G.; Lauerwald, R.; Luyssaert, S.; Andersson, A.J. Anthropogenic perturbation of the carbon fluxes from land to ocean. *Nat. Geosci.* **2013**, *6*, 597–607. [CrossRef]
191. Xu, J.; Lei, S.; Bi, S.; Li, Y.; Lyu, H.; Xu, J.; Xu, X.; Mu, M.; Miao, S.; Zeng, S.; et al. Tracking spatio-temporal dynamics of POC sources in eutrophic lakes by remote sensing. *Water Res.* **2020**, *168*, 115162. [CrossRef]
192. Wei, X.; Shen, F.; Pan, Y.; Chen, S.; Sun, X.; Wang, Y. Satellite Observations of the Diurnal Dynamics of Particulate Organic Carbon in Optically Complex Coastal Oceans: The Continental Shelf Seas of China. *J. Geophys. Res. Ocean.* **2019**, *124*, 4710–4726. [CrossRef]
193. Catalán, N.; Obrador, B.; Alomar, C.; Pretus, J.L. Seasonality and landscape factors drive dissolved organic matter properties in Mediterranean ephemeral washes. *Biogeochemistry* **2012**, *112*, 261–274. [CrossRef]
194. Fichot, C.G.; Tzortziou, M.; Mannino, A. Remote sensing of dissolved organic carbon (DOC) stocks, fluxes and transformations along the land-ocean aquatic continuum: Advances, challenges, and opportunities. *Earth-Sci. Rev.* **2023**, *242*, 104446. [CrossRef]
195. Huang, C.; Yunmei, L.; Liu, G.; Guo, Y.; Yang, H.; Zhu, A.X.; Song, T.; Huang, T.; Zhang, M.; Shi, K. Tracing high time-resolution fluctuations in dissolved organic carbon using satellite and buoy observations: Case study in Lake Taihu, China. *Int. J. Appl. Earth Obs. Geoinf.* **2017**, *62*, 174–182. [CrossRef]
196. Gomes, H.d.R.; Xu, Q.; Ishizaka, J.; Carpenter, E.J.; Yager, P.L.; Goes, J.I. The influence of riverine nutrients in niche partitioning of phytoplankton communities—A contrast between the Amazon River Plume and the ChangJiang (Yangtze) River diluted water of the East China Sea. *Front. Mar. Sci.* **2018**, *5*, 343. [CrossRef]
197. Reid, P.C.; Fischer, A.C.; Lewis-Brown, E.; Meredith, M.P.; Sparrow, M.; Andersson, A.J.; Antia, A.; Bates, N.R.; Bathmann, U.; Beaugrand, G. Impacts of the oceans on climate change. *Adv. Mar. Biol.* **2009**, *56*, 1–150. [PubMed]
198. Wu, J.; Goes, J.I.; do Rosario Gomes, H.; Lee, Z.; Noh, J.-H.; Wei, J.; Shang, Z.; Salisbury, J.; Mannino, A.; Kim, W. Estimates of diurnal and daily net primary productivity using the Geostationary Ocean Color Imager (GOCI) data. *Remote Sens. Environ.* **2022**, *280*, 113183. [CrossRef]
199. Cui, H.; Chen, J.; Cao, Z.; Huang, H.; Gong, F. A Novel Multi-Candidate Multi-Correlation Coefficient Algorithm for GOCI-Derived Sea-Surface Current Vector with OSU Tidal Model. *Remote Sens.* **2022**, *14*, 4625. [CrossRef]
200. Sun, D.; Su, X.; Qiu, Z.; Wang, S.; Mao, Z.; He, Y. Remote sensing estimation of sea surface salinity from GOCI measurements in the southern Yellow Sea. *Remote Sens.* **2019**, *11*, 775. [CrossRef]
201. Lee, H.-S.; Lee, K.-S. Capability of geostationary satellite imagery for sea ice monitoring in the Bohai and Yellow seas. *J. Mar. Sci. Technol.* **2016**, *24*, 10.
202. Gu, F.; Zhang, R.; Tian-Kunze, X.; Han, B.; Zhu, L.; Cui, T.; Yang, Q. Sea Ice Thickness Retrieval Based on GOCI Remote Sensing Data: A Case Study. *Remote Sens.* **2021**, *13*, 936. [CrossRef]
203. Yan, Y.; Huang, K.; Shao, D.; Xu, Y.; Gu, W. Monitoring the Characteristics of the Bohai Sea Ice Using High-Resolution Geostationary Ocean Color Imager (GOCI) Data. *Sustainability* **2019**, *11*, 777. [CrossRef]

204. Zhou, Y.; Chen, K.; Li, X. Dual-branch neural network for sea fog detection in geostationary ocean color imager. *IEEE Trans. Geosci. Remote Sens.* **2022**, *60*, 4208617. [CrossRef]
205. Jeon, H.-K.; Kim, S.; Edwin, J.; Yang, C.-S. Sea fog identification from GOCI images using CNN transfer learning models. *Electronics* **2020**, *9*, 311. [CrossRef]
206. Arp, C.D.; Cherry, J.E.; Brown, D.; Bondurant, A.C.; Endres, K.L. Observation-derived ice growth curves show patterns and trends in maximum ice thickness and safe travel duration of Alaskan lakes and rivers. *Cryosphere* **2020**, *14*, 3595–3609. [CrossRef]
207. Pearce, D.A. Antarctic subglacial lake exploration: A new frontier in microbial ecology. *ISME J.* **2009**, *3*, 877–880. [CrossRef] [PubMed]
208. Hampton, S.E.; Galloway, A.W.; Powers, S.M.; Ozersky, T.; Woo, K.H.; Batt, R.D.; Labou, S.G.; O'Reilly, C.M.; Sharma, S.; Lottig, N.R. Ecology under lake ice. *Ecol. Lett.* **2017**, *20*, 98–111. [CrossRef] [PubMed]
209. Yang, H.; Kong, J.; Hu, H.; Du, Y.; Gao, M.; Chen, F. A review of remote sensing for water quality retrieval: Progress and challenges. *Remote Sens.* **2022**, *14*, 1770. [CrossRef]
210. Kirk, J. Dependence of relationship between inherent and apparent optical properties of water on solar altitude. *Limnol. Oceanogr.* **1984**, *29*, 350–356. [CrossRef]
211. Kirk, J.T. Volume scattering function, average cosines, and the underwater light field. *Limnol. Oceanogr.* **1991**, *36*, 455–467. [CrossRef]
212. McKee, D.; Cunningham, A.; Dudek, A. Optical water type discrimination and tuning remote sensing band-ratio algorithms: Application to retrieval of chlorophyll and Kd (490) in the Irish and Celtic Seas. *Estuar. Coast. Shelf Sci.* **2007**, *73*, 827–834. [CrossRef]
213. Zhang, Y.; Xu, Z.; Yang, Y.; Wang, G.; Zhou, W.; Cao, W.; Li, Y.; Zheng, W.; Deng, L.; Zeng, K. Diurnal variation of the diffuse attenuation coefficient for downwelling irradiance at 490 nm in coastal East China Sea. *Remote Sens.* **2021**, *13*, 1676. [CrossRef]
214. Yu, X.; Salama, M.S.; Shen, F.; Verhoef, W. Retrieval of the diffuse attenuation coefficient from GOCI images using the 2SeaColor model: A case study in the Yangtze Estuary. *Remote Sens. Environ.* **2016**, *175*, 109–119. [CrossRef]
215. Tang, R.; Shen, F.; Pan, Y.; Ruddick, K.; Shang, P. Multi-source high-resolution satellite products in Yangtze Estuary: Cross-comparisons and impacts of signal-to-noise ratio and spatial resolution. *Opt. Express* **2019**, *27*, 6426–6441. [CrossRef] [PubMed]
216. Hu, C.; Feng, L.; Lee, Z. Evaluation of GOCI sensitivity for at-sensor radiance and GDPS-retrieved chlorophyll-a products. *Ocean Sci. J.* **2012**, *47*, 279–285. [CrossRef]
217. Qi, L.; Lee, Z.; Hu, C.; Wang, M. Requirement of minimal signal-to-noise ratios of ocean color sensors and uncertainties of ocean color products. *J. Geophys. Res. Ocean.* **2017**, *122*, 2595–2611. [CrossRef]
218. Bi, S.; Röttgers, R.; Hieronymi, M. Transfer model to determine the above-water remote-sensing reflectance from the underwater remote-sensing ratio. *Opt. Express* **2023**, *31*, 10512–10524. [CrossRef]
219. Xu, F.; He, X.; Jin, X.; Cai, W.; Bai, Y.; Wang, D.; Gong, F.; Zhu, Q. Spherical vector radiative transfer model for satellite ocean color remote sensing. *Opt. Express* **2023**, *31*, 11192–11212. [CrossRef] [PubMed]
220. Prakash, W.; Varma, A.; Bhandari, S. An algorithm for the precise location of the solar specular reflection point in the visible band images from geostationary meteorological satellites. *Comput. Geosci.* **1994**, *20*, 1467–1482. [CrossRef]
221. Wu, X.; Lu, Y.; Jiao, J.; Ding, J.; Fu, W.; Qian, W. Using sea wave simulations to interpret the sunglint reflection variation with different spatial resolutions. *IEEE Geosci. Remote Sens. Lett.* **2020**, *19*, 1501304. [CrossRef]
222. Park, Y.; Ahn, Y.; Han, H.; Yang, H.; Moon, J.; Ahn, J.; Lee, B.; Min, J.; Lee, S.; Kim, K. *GOCI Level 2 Ocean Color Products (GDPS 1.3) Brief Algorithm Description*; Korea Ocean Satellite Center (KOSC): Ansan, Republic of Korea, 2014; pp. 24–40.
223. Kim, Y.J.; Kim, W.; Im, J.; Choi, J.; Lee, S. Atmospheric-correction-free red tide quantification algorithm for GOCI based on machine learning combined with a radiative transfer simulation. *ISPRS J. Photogramm. Remote Sens.* **2023**, *199*, 197–213. [CrossRef]
224. Mao, K.; Yuan, Z.; Zuo, Z.; Xu, T.; Shen, X.; Gao, C. Changes in global cloud cover based on remote sensing data from 2003 to 2012. *Chin. Geogr. Sci.* **2019**, *29*, 306–315. [CrossRef]
225. Colomina, I.; Molina, P. Unmanned aerial systems for photogrammetry and remote sensing: A review. *ISPRS J. Photogramm. Remote Sens.* **2014**, *92*, 79–97. [CrossRef]
226. Kwon, D.Y.; Kim, J.; Park, S.; Hong, S. Advancements of remote data acquisition and processing in unmanned vehicle technologies for water quality monitoring: An extensive review. *Chemosphere* **2023**, *343*, 140198. [CrossRef] [PubMed]
227. Yuan, S.; Li, Y.; Bao, F.; Xu, H.; Yang, Y.; Yan, Q.; Zhong, S.; Yin, H.; Xu, J.; Huang, Z. Marine environmental monitoring with unmanned vehicle platforms: Present applications and future prospects. *Sci. Total Environ.* **2023**, *858*, 159741. [CrossRef]
228. Zhao, H.; Zhou, Y.; Wu, H.; Kutser, T.; Han, Y.; Ma, R.; Yao, Z.; Zhao, H.; Xu, P.; Jiang, C. Potential of Mie–fluorescence–Raman lidar to profile chlorophyll a concentration in inland waters. *Environ. Sci. Technol.* **2023**, *57*, 14226–14236. [CrossRef] [PubMed]
229. Wang, W.; Shi, K.; Zhang, Y.; Li, N.; Sun, X.; Zhang, D.; Zhang, Y.; Qin, B.; Zhu, G. A ground-based remote sensing system for high-frequency and real-time monitoring of phytoplankton blooms. *J. Hazard. Mater.* **2022**, *439*, 129623. [CrossRef] [PubMed]
230. Wang, X.; Wang, W.; He, Y.; Zhang, S.; Huang, W.; Woolway, R.I.; Shi, K.; Yang, X. Numerical simulation of thermal stratification in Lake Qiandaohu using an improved WRF-Lake model. *J. Hydrol.* **2023**, *618*, 129184. [CrossRef]
231. Li, Y.; Li, Y.-M.; Wang, Q.; Zhu, L.; Guo, Y.-L. An Observing System Simulation Experiments framework based on the ensemble square root Kalman Filter for evaluating the concentration of chlorophyll a by multi-source data: A case study in Taihu Lake. *Aquat. Ecosyst. Health Manag.* **2014**, *17*, 233–241. [CrossRef]

232. Guo, Y.; Li, Y.; Zhu, L.; Wang, Q.; Lv, H.; Huang, C.; Li, Y. An inversion-based fusion method for inland water remote monitoring. *IEEE J. Sel. Top. Appl. Earth Obs. Remote Sens.* **2016**, *9*, 5599–5611. [CrossRef]
233. Murakami, H. Ocean color estimation by Himawari-8/AHI. In Proceedings of the Remote Sensing of the Oceans and Inland Waters: Techniques, Applications, and Challenges, New Delhi, India, 4–7 April 2016; pp. 177–186.
234. Guo, Y.; Huang, C.; Zhang, Y.; Li, Y.; Chen, W. A novel multitemporal image-fusion algorithm: Method and application to GOCI and himawari images for inland water remote sensing. *IEEE Trans. Geosci. Remote Sens.* **2020**, *58*, 4018–4032. [CrossRef]
235. Chang, N.-B.; Vannah, B.; Yang, Y.J. Comparative sensor fusion between hyperspectral and multispectral satellite sensors for monitoring microcystin distribution in Lake Erie. *IEEE J. Sel. Top. Appl. Earth Obs. Remote Sens.* **2014**, *7*, 2426–2442. [CrossRef]
236. Mélin, F.; Zibordi, G. Optically based technique for producing merged spectra of water-leaving radiances from ocean color remote sensing. *Appl. Opt.* **2007**, *46*, 3856–3869. [CrossRef] [PubMed]
237. Mélin, F.; Zibordi, G.; Djavidnia, S. Merged series of normalized water leaving radiances obtained from multiple satellite missions for the Mediterranean Sea. *Adv. Space Res.* **2009**, *43*, 423–437. [CrossRef]
238. Mélin, F.; Vantrepotte, V.; Chuprin, A.; Grant, M.; Jackson, T.; Sathyendranath, S. Assessing the fitness-for-purpose of satellite multi-mission ocean color climate data records: A protocol applied to OC-CCI chlorophyll-a data. *Remote Sens. Environ.* **2017**, *203*, 139–151. [CrossRef]
239. Cao, Z.; Duan, H.; Shen, M.; Ma, R.; Xue, K.; Liu, D.; Xiao, Q. Using VIIRS/NPP and MODIS/Aqua data to provide a continuous record of suspended particulate matter in a highly turbid inland lake. *Int. J. Appl. Earth Obs. Geoinf.* **2018**, *64*, 256–265. [CrossRef]
240. Cao, F.; Miller, W.L. A new algorithm to retrieve chromophoric dissolved organic matter (CDOM) absorption spectra in the UV from ocean color. *J. Geophys. Res. Ocean.* **2015**, *120*, 496–516. [CrossRef]
241. He, X.; Bai, Y.; Pan, D.; Tang, J.; Wang, D. Atmospheric correction of satellite ocean color imagery using the ultraviolet wavelength for highly turbid waters. *Opt. Express* **2012**, *20*, 20754–20770. [CrossRef] [PubMed]
242. Werdell, P.J.; Bailey, S.W.; Franz, B.A.; Harding, L.W., Jr.; Feldman, G.C.; McClain, C.R. Regional and seasonal variability of chlorophyll-a in Chesapeake Bay as observed by SeaWiFS and MODIS-Aqua. *Remote Sens. Environ.* **2009**, *113*, 1319–1330. [CrossRef]
243. Simis, S.G.; Peters, S.W.; Gons, H.J. Remote sensing of the cyanobacterial pigment phycocyanin in turbid inland water. *Limnol. Oceanogr.* **2005**, *50*, 237–245. [CrossRef]
244. Liu, G.; Simis, S.G.; Li, L.; Wang, Q.; Li, Y.; Song, K.; Lyu, H.; Zheng, Z.; Shi, K. A four-band semi-analytical model for estimating phycocyanin in inland waters from simulated MERIS and OLCI data. *IEEE Trans. Geosci. Remote Sens.* **2017**, *56*, 1374–1385. [CrossRef]
245. Lyu, L.; Song, K.; Wen, Z.; Liu, G.; Fang, C.; Shang, Y.; Li, S.; Tao, H.; Wang, X.; Li, Y. Remote estimation of phycocyanin concentration in inland waters based on optical classification. *Sci. Total Environ.* **2023**, *899*, 166363. [CrossRef] [PubMed]
246. Kwon, Y.S.; Pyo, J.; Kwon, Y.-H.; Duan, H.; Cho, K.H.; Park, Y. Drone-based hyperspectral remote sensing of cyanobacteria using vertical cumulative pigment concentration in a deep reservoir. *Remote Sens. Environ.* **2020**, *236*, 111517. [CrossRef]
247. Pyo, J.; Duan, H.; Baek, S.; Kim, M.S.; Jeon, T.; Kwon, Y.S.; Lee, H.; Cho, K.H. A convolutional neural network regression for quantifying cyanobacteria using hyperspectral imagery. *Remote Sens. Environ.* **2019**, *233*, 111350. [CrossRef]
248. Shen, M.; Cao, Z.; Xie, L.; Zhao, Y.; Qi, T.; Song, K.; Lyu, L.; Wang, D.; Ma, J.; Duan, H. Microcystins risk assessment in lakes from space: Implications for SDG 6.1 evaluation. *Water Res.* **2023**, *245*, 120648. [CrossRef] [PubMed]
249. Liu, G.; Li, L.; Song, K.; Li, Y.; Lyu, H.; Wen, Z.; Fang, C.; Bi, S.; Sun, X.; Wang, Z. An OLCI-based algorithm for semi-empirically partitioning absorption coefficient and estimating chlorophyll a concentration in various turbid case-2 waters. *Remote Sens. Environ.* **2020**, *239*, 111648. [CrossRef]
250. Gitelson, A.A.; Dall'Olmo, G.; Moses, W.; Rundquist, D.C.; Barrow, T.; Fisher, T.R.; Gurlin, D.; Holz, J. A simple semi-analytical model for remote estimation of chlorophyll-a in turbid waters: Validation. *Remote Sens. Environ.* **2008**, *112*, 3582–3593. [CrossRef]
251. Bai, R.; He, X.; Bai, Y.; Gong, F.; Zhu, Q.; Wang, D.; Li, T. Atmospheric correction algorithm based on the interpolation of ultraviolet and shortwave infrared bands. *Opt. Express* **2023**, *31*, 6805–6826. [CrossRef] [PubMed]
252. Pi, X.; Luo, Q.; Feng, L.; Xu, Y.; Tang, J.; Liang, X.; Ma, E.; Cheng, R.; Fensholt, R.; Brandt, M. Mapping global lake dynamics reveals the emerging roles of small lakes. *Nat. Commun.* **2022**, *13*, 5777. [CrossRef]
253. Tao, H.; Song, K.; Liu, G.; Wen, Z.; Wang, Q.; Du, Y.; Lyu, L.; Du, J.; Shang, Y. Songhua River basin's improving water quality since 2005 based on Landsat observation of water clarity. *Environ. Res.* **2021**, *199*, 111299. [CrossRef]
254. Ani, C.J.; Baird, M.; Robson, B. Modelling buoyancy-driven vertical movement of Trichodesmium application in the Great Barrier Reef. *Ecol. Model.* **2024**, *487*, 110567. [CrossRef]
255. Wen, Z.; Shang, Y.; Lyu, L.; Tao, H.; Liu, G.; Fang, C.; Li, S.; Song, K. Re-estimating China's lake CO_2 flux considering spatiotemporal variability. *Environ. Sci. Ecotechnology* **2024**, *19*, 100337. [CrossRef] [PubMed]
256. Sommerfield, C.K.; Wong, K.C. Mechanisms of sediment flux and turbidity maintenance in the Delaware Estuary. *J. Geophys. Res. Ocean.* **2011**, *116*, C01005. [CrossRef]
257. Uncles, R.; Elliott, R.; Weston, S. Observed fluxes of water, salt and suspended sediment in a partly mixed estuary. *Estuar. Coast. Shelf Sci.* **1985**, *20*, 147–167. [CrossRef]
258. Li, Y.; Robinson, S.V.; Nguyen, L.H.; Liu, J. Satellite prediction of coastal hypoxia in the northern Gulf of Mexico. *Remote Sens. Environ.* **2023**, *284*, 113346. [CrossRef]

259. Hu, C.; Lu, Y.; Sun, S.; Liu, Y. Optical remote sensing of oil spills in the ocean: What is really possible? *J. Remote Sens.* **2021**, *2021*, 9141902. [CrossRef]
260. Sun, Z.; Sun, S.; Zhao, J.; Ai, B.; Yang, Q. Detection of Massive Oil Spills in Sun Glint Optical Imagery through Super-Pixel Segmentation. *J. Mar. Sci. Eng.* **2022**, *10*, 1630. [CrossRef]
261. Jiao, J.; Lu, Y.; Liu, Y. Optical quantification of oil emulsions in multi-band coarse-resolution imagery using a lab-derived HSV model. *Mar. Pollut. Bull.* **2022**, *178*, 113640. [CrossRef]
262. Raffaelli, D.G.; Hawkins, S.J. *Intertidal Ecology*; Springer Science & Business Media: Berlin/Heidelberg, Germany, 1996.
263. Jia, M.; Wang, Z.; Mao, D.; Ren, C.; Wang, C.; Wang, Y. Rapid, robust, and automated mapping of tidal flats in China using time series Sentinel-2 images and Google Earth Engine. *Remote Sens. Environ.* **2021**, *255*, 112285. [CrossRef]
264. Kennedy, V.S.; Newell, R.I.; Shumway, S. Natural environmental factors. In *The Eastern Oyster Crassostrea virginica*; Maryland Sea Grant: College Park, MD, USA, 1996; pp. 467–513.